2019

An Analysis of Fractures around the Sevier Fault Zone near Orderville, Utah

Charley H. Hankla
The College of Wooster, chankla19@wooster.edu

An Analysis of Fractures around the Sevier Fault Zone near Orderville, Utah

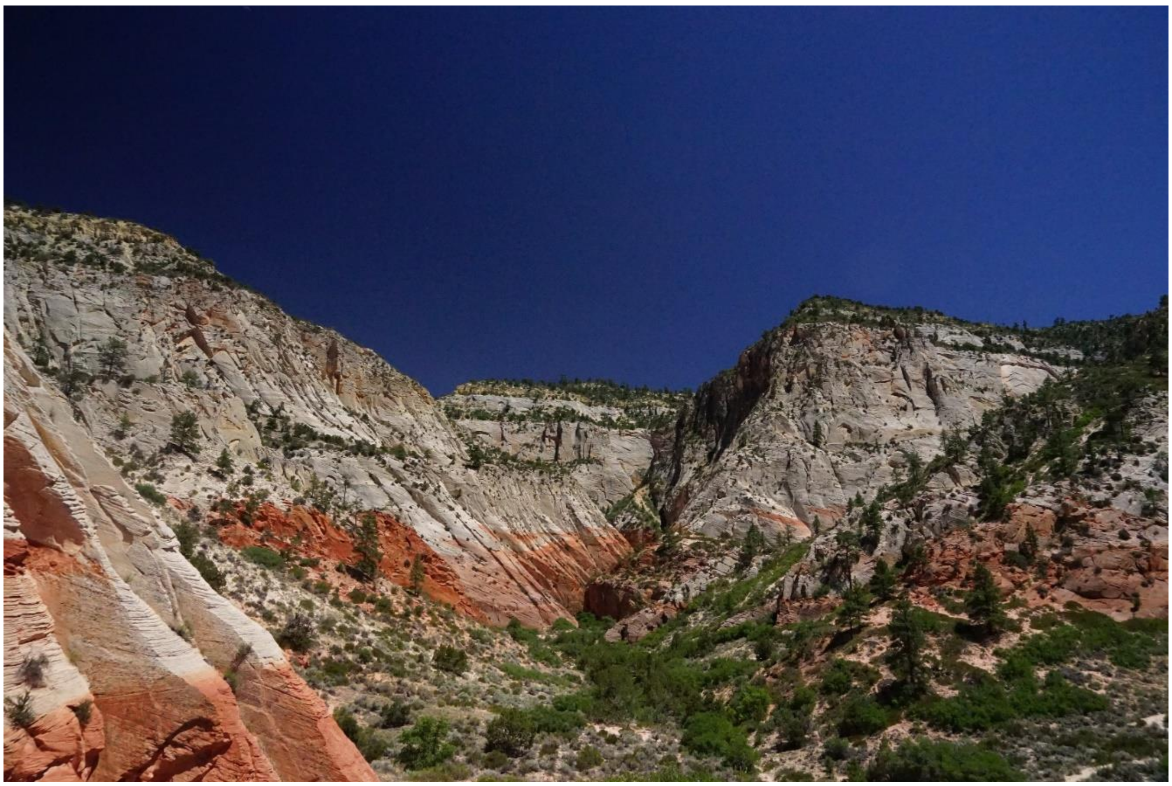

by

Charley H. Hankla

Submitted in partial fulfillment of the requirements
of Senior Independent Study
at The College of Wooster

March 6, 2019

Cover photo: 2018 Utah scenic shot DS05620. Photo credit: Ben Surpless.

Abstract

Structural discontinuities—such as opening mode joints, shear fractures, and faults— tend to occur in close geographic proximity to one another; however, the timing relationships between these structures is not always easy to discern in the field. In southwestern Utah, the Jurassic Navajo Sandstone is cut by large-scale normal faults associated with the Sevier Fault Zone, making it perfect for observing several fracture types. The aim of this study is to complete a dynamic and kinematic analyses of the fractures near a major fault and to determine the chronologic relationships between the fractures. Specifically, we observed a previously unnamed segment of the Sevier Fault Zone— herein referred to as the Mountain Lion Den Fault— previously interpreted as a west dipping normal fault striking 030. The primary field area is the Red Hollow Canyon/Elkheart Cliffs region, located southeast of Orderville, Utah.

For this study, orientations (dip and dip direction) of fracture data within the Navajo Sandstone were measured and tracked on eight different scanlines. Scanline fractures were plotted on stereonets and averages determined. GPS locations were taken on a Trimble G7X at ends of each scanline for GIS mapping. Schmidt Hammer (L-type) data were taken to compare rock strengths near the Mountain Lion Den Fault.

Fracture analyses show a general NNE strike similar to the Mountain Lion Den fault strike. Despite a few outliers, scanline averages typically strike within 10° of the 030 strike of the Mountain Lion Den fault. We interpret movement along the fault initiated around the same time some of the fractures formed. The fractures likely formed in front of the Mountain Lion Den fault at oblique angles to its strike as the fault propagated northward. These results suggest that an area of weakness formed in Red Hollow Canyon, allowing the fault to propagate easily at 030. This compares favorably to previous brittle fracture studies within

propagating fault zones. Outliers in the data could be associated with NW rotation of σ3, similar to joints in Zion NP. Schmidt Hammer data show that oxidized beds have greater maximum compressive strengths than bleached zones in the Navajo Sandstone.

Acknowledgements

This material is based upon work supported by the Keck Geology Consortium and the National Science Foundation under Grant No. 1659322.

This would not have happened without the Wooster Earth Sciences Department; faculty, staff, and students. You all have been so supportive and helpful throughout my time here. My advisor, Dr. Shelley Judge, has helped immensely with so many things and I definitely would not have gotten here without her.

I would like to thank the Keck Utah Squad- Dr. Ben Surpless, Madison, Caroline, and Curtis- for an amazing field experience, my family for their constant support through the ups and downs of the IS journey, and my friends for being there for me for anything.

My IS is dedicated to my grandmother, Alice Clair Kimbler Hankla. She will never get to read this, but she has always been supportive of my scientific endeavors. Look, Grandmom, I made it!

Thank you for everything

Contents

Introduction

Importance

The study of fractures in the Navajo Sandstone is important for understanding and predicting fluid flow. The Navajo Sandstone is the most porous formation in the region and is covered by capping sediments. The vast majority of the sandstone is well sorted quartz grains from very fine to medium grained in size. Fractures affect the ease that fluids flow in rocks; they can either increase or decrease the permeability. If the fractures are deformation bands, fluid flow is majorly hindered. Other fractures, especially opening, can increase fluid flow. Understanding how fractures form can help geologists predict how fluid flow will be affected, as well as fault locations and types. Since the Navajo Sandstone is overlain by the Temple Cap and Twin Creek members that act as caps, fluid can be trapped in areas of the Navajo. Fractures are found to increase in abundance closer to faults, so faults that cut through reservoirs majorly affect the movement of fluids (Chidsey et al., 2007; Fossen and Bale, 2007; Fossen, 2010; Fossen et al., 2011).

Keck Geology Consortium

The Keck Geology Consortium is a group of 17 liberal arts colleges focused on enhancing students' education through high caliber Research Experiences for Undergraduates–known as REUs. Students participate in four to five week projects that consist of lab and field research. For advanced students, i.e. rising seniors, the research usually leads to a senior thesis and presentation at a professional conference. Macalester College currently runs the Keck Geology Consortium that is funded by the NSF (Keck Geology Consortium, 2018).

This study is based upon the data obtained on a research trip that was led by Dr. Ben Surpless of Trinity University. Caroline McKeighan, Curtis Segarra, Madison Woodley, and I accompanied him. Caroline and Curtis are both senior geology majors from Trinity, and Madison is a senior geology major from Mount Holyoke College. They are all also using the data collected in the field to complete a senior project at their respective institutions (Surpless, 2017, 2018).

Objectives

The aims of this study are to:

- Describe fracture morphologies and orientations (kinematic analysis)
- Map the spatial relationships between the fractures and the local normal faults
- Analyze fracture relationships to the nearby normal fault zone
- Determine the orientation of the regional stress regime (dynamic analysis)

Location

This study is focused on Red Hollow Canyon and Elkheart Cliffs in southwestern Utah because of the great exposures of the Navajo Sandstone around faulted areas. These locations are close to Orderville, UT, which is accessible from the north and south via Highway 89. Northerly tilting strata on a hill can be seen to the right as one drives into Orderville from the south and represents the relay ramp that marks the entrance to Red Hollow Canyon. Highway 89 runs along the western side of a large, eroded valley. Orderville is located at 37°15’44 N, 112°39’12” W and is on the eastern side of the transition zone between the Colorado Plateau and the Basin and Range physiographic provinces (Eaton, 1982; Moores and Twiss, 1995; "Orderville, Utah," 2018).

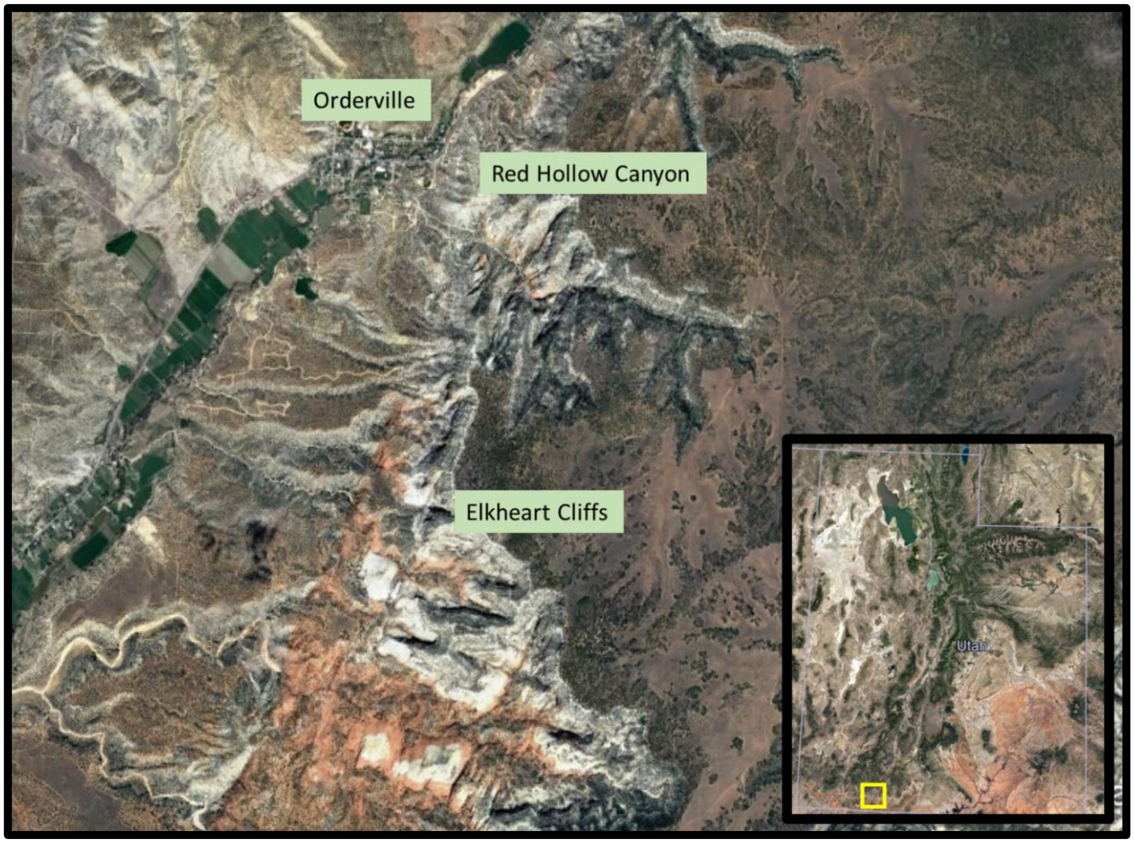

Figure 1: Satellite imagery of study locations. Inset is a larger scale map of Utah ("Google Earth Pro v. 7.3.2, imagery 7/22/2015, 2019 Google").

Background

Tectonic Setting

In the western states of the US, there are multiple different areas of distinct geology called physiographic provinces. Starting in the east, the Colorado Plateau is a sprawling province that is defined by the fact that it has not undergone any massive deformation events. Therefore, the Plateau has very little topographic relief and the majority of the sediments are flat lying. Marked by changes in deformation, volcanism, topography, and crustal structure, the

Colorado Plateau gradually gives way to the Basin and Range physiographic province in the west (Jackson, 1990b, 1990a; Porter et al., 2017). This massive province extends about 3,700 km from Mexico to Canada and is the result of large scale extension that began in the Oligocene. Elongate valleys, north to north-northeast trending mountain ranges, and gently dipping strata are characteristic of the area. The extension produced a large, consistent series of horsts and grabens as well as a variety of other structures including fractures and relay ramps (Stewart, 1998). Changes from one province to another are not sudden, so between the two is the 150 km wide Transition Zone. It contains characteristics from both provinces and is thought to have started forming when the extension began, around 29 Ma. The modern topographies and plateaus visible in Utah are predicted to be younger than 14 Ma, indicating that the extension is likely ongoing (Eaton, 1982; Stewart, 1998).

Geologic Setting

Within the Basin and Range and Transition Zone provinces, there are many normal faults to accommodate the strain from the regional extension. Specifically, in southern Utah there are four main faults or fault zones: the Grand Wash Fault Zone, the Hurricane Fault, the Sevier Fault Zone, and the Paunsaugunt Fault. This study focuses on the Sevier Fault Zone, near Orderville, Utah. It is called a fault zone because there is not just one but many fault segments that contribute to accommodating the offset from regional extension. The segments in the Sevier Fault Zone are high angle normal faults with a total trace length of about 100 km and generally striking 030, dipping west. This zone started faulting around 15 to 12 Ma and has produced two recorded earthquakes, implying that it is still active (Eaton, 1982; Moores and Twiss, 1995; Davis, 1999).

Data collection for this study occurred along the Elkheart Cliffs Fault, Mountain Lion Den Fault, and a potential small fault segment crossing the canyon between the Mountain Lion Den and Elkheart Cliffs Faults (Doelling, 2008), which strikes at 025 and will be referred to as the Kimbler Fault. An additional area of major deformation is in the eastern portion of the canyon, likely just a heavily fractured zone because no offset was observed. West of Red Hollow Canyon is a fault that forms the Orderville Relay Ramp with the Elkheart Cliffs Fault and briefly follows Highway 89, to be referred to as the Highway 89 Fault. Major faults labelled in Figure 2.

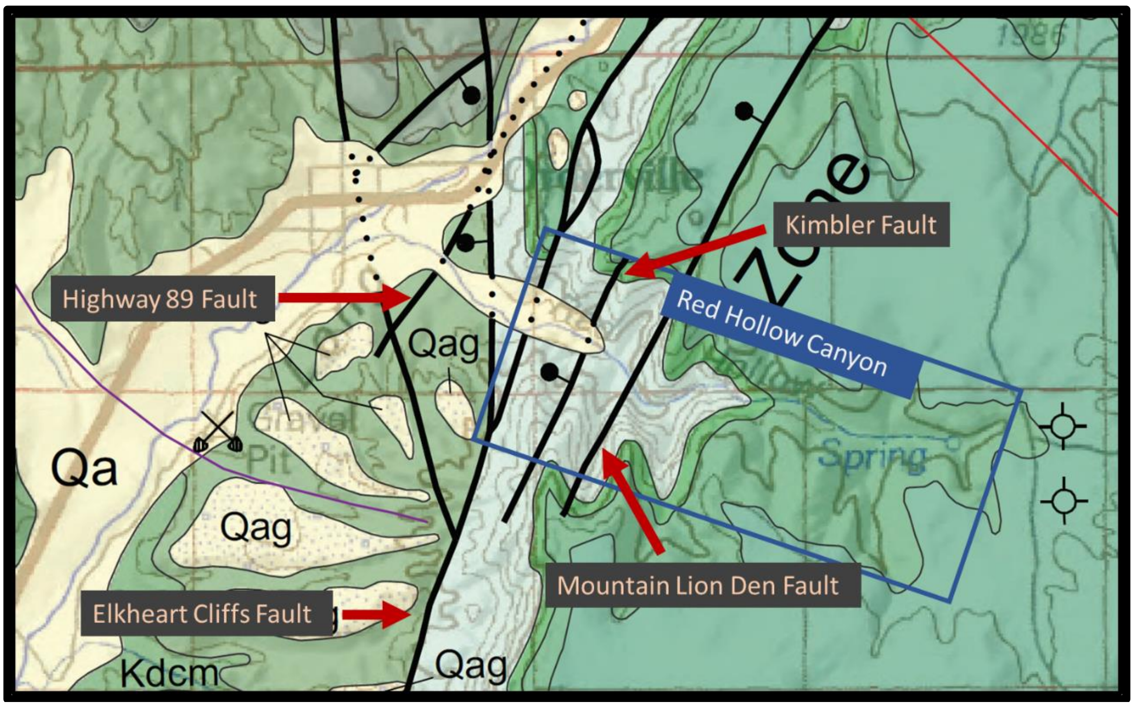

Figure 2: Geologic map of the portion of the Sevier Fault Zone in which the study was conducted. Red Hollow Canyon emphasized with blue box (Modified from Doelling, 2008).

Stratigraphy

The Navajo Sandstone is a well exposed, Early Jurassic erg unit that extends from present day Arizona to Wyoming. It is the most porous sandstone in the region (Chidsey et al., 2007; Fossen, 2010; Fossen et al., 2011). The sand was deposited in eolian dunes, making structures like foresets and cross-bedding a common occurrence. Possible origins for the sand include exposed sandstones of Paleozoic to Triassic age found in Canada and sediments from as far east as the Appalachian area. These sediments mixed with others from local sources as they moved southwest before settling in the vast desert that makes up the Navajo. Sand grains within the sandstone are generally well sorted, very fine to medium grained, and subrounded to subangular. Quartz makes up 97% of the formation, with some chert nodules, K-feldspar, and lithics present (Peterson and Pipiringos, 1979; Chidsey et al., 2007; Doelling, 2008).

Structures

Fractures

Fractures are planar features that form to help accommodate stress. There are three main modes of fracturing; Mode 1 are opening fractures also called joints, Mode 2 is sliding, and Mode 3 is tearing. For dip-slip faults, Mode 2 tends to be on the top and bottom tips of fault planes and fractures on the lateral tips tend to be Mode 3, however, these can occur simultaneously to Mode 1, creating zones of mixed mode fracturing (McGrath and Davison, 1995). Indicators of fractures in the field include extremely flat faces along exposures, cracks in an outcrop, hackle plume structures, and arrest lines.

Transfer Zones

Transfer zones, also known as accommodation zones, are areas between faults that overlap in map view. The overstepping faults can either be dipping in the same or different directions. When normal overlapping faults are dipping in the same direction, they are called synthetic accommodation zones and relay ramps form, helping accommodate additional stress. In mature relay ramps, the ramp has been breached, or connected, by faults subperpendicular to the main faults, Figure 3c. When the overlapping faults are dipping in opposite directions, transfer zones are called antithetic accommodation zones. Antithetic transfer zones are home to a wide range of geometries, including anticlines and synclines (Faulds and Varga, 1998). Just to the west of the study area, there is a fantastically exposed relay ramp called the Orderville Relay Ramp that connects the Elkheart Cliffs and Highway 89 Faults (Schiefelbein, 2002; Doelling, 2008).

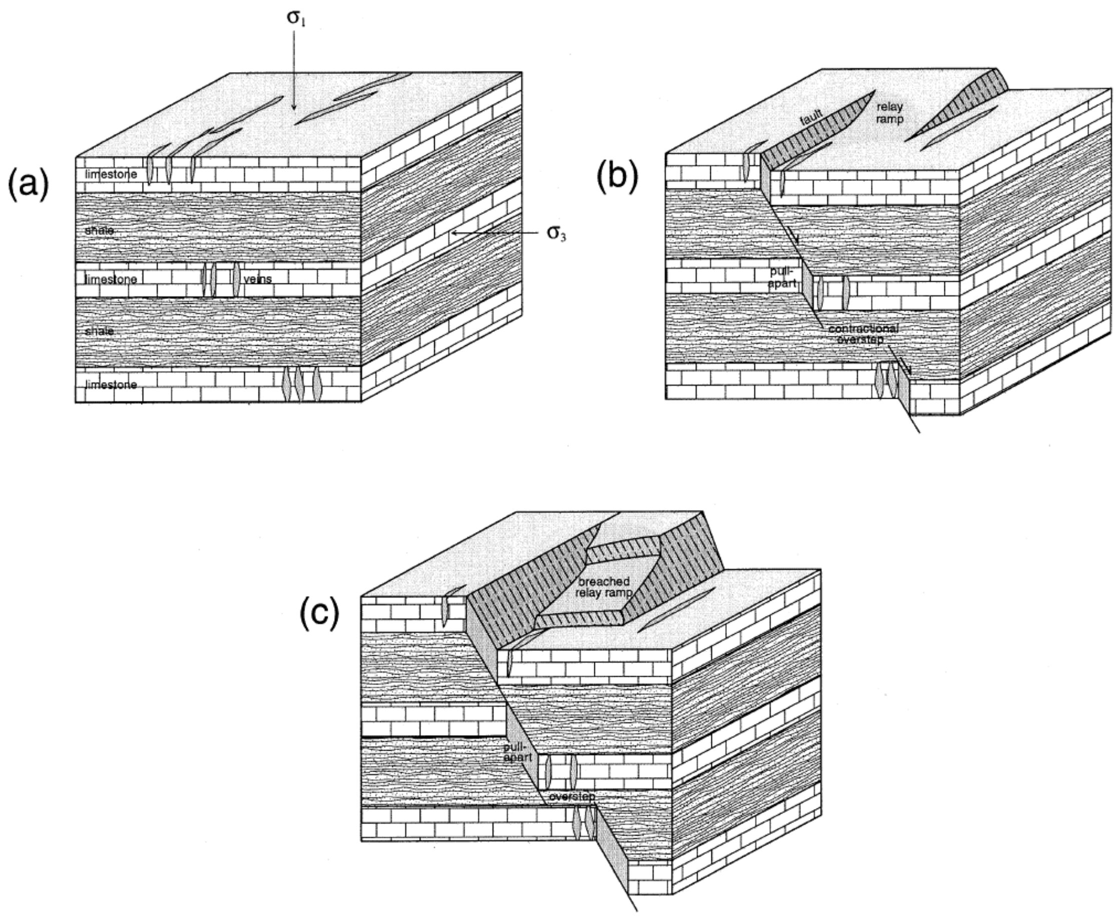

Figure 3: Block diagrams illustrating the formation of relay ramps. (a) fractures develop in the brittle layers; (b) extension continues, causing the onset of faulting along the fracture strikes as well as the beginning of a relay ramp between overstepping faults; (c) overstepping segments of the developing faults connect in the subsurface and breach the top and bottom of the relay ramp as more extension occurs (From Peacock, 2002, Figure 3).

Methods

Fracture Data

When determining if a fracture's attitude was to be recorded, its length and accessibility were considered. If the visible portion of the fracture extended less than 4 meters (12 feet), it was not measured. Fractures that were inaccessible in the field were also skipped, leaving gaps in some of the scanlines. On viable fractures, Brunton compasses were used to determine the dip and dip direction, by putting the back of the compass directly on the fracture plane. If the fracture plane did not have enough room for a compass, a map board was used to extend the fracture out so that a measurement could be recorded. Once leveled, the azimuthal orientation was taken for the dip direction and the dip angle was taken from the side of the compass. Fractures that were similar in their attitude to the first fracture on the scanline they were on are labeled as 'typical' fractures and those varying from the typical are called 'diamond' fractures. Disclaimer: fracture orientation data were collected by multiple students in the field, so there may be some inconsistencies. The worry with the dataset is the possibility that not all dip directions were recorded correctly, however, the data that we collected in the field will still be used for this study.

Scanlines

While moving through the canyons and taking fracture data, scanlines were also recorded. Scanlines, for the purposes of this study, are used to measure total distance travelled, approximately perpendicular to the exposure. To make the scanlines, measurements in meters were recorded using a large tape measure between each viable fracture. To keep a consistent orientation of the line, some fractures were visually extended out from the exposure to allow the measuring tape to reach the next fracture. GPS locations were taken on a Trimble G7X whenever a day in the field began or ended, at any particularly interesting feature, at photo locations, at sample locations, every so often just in case, and where scanlines were started or stopped.

A scanline with fractures on it can be constructed using the distance measurements between fractures. Distance measurements were only taken between typical fractures. There are large gaps in some of the scanlines, indicating the absence of viable fractures or the lack of accessible outcrops. Several gaps, especially in scanline A, represent areas of debris and erosional sediment that prevented fractures from being seen. Eight scanlines were taken in total while in the field; five in Red Hollow Canyon and three in Elkheart Cliffs.

Schmidt Hammer Data

At every sturdy sample location, except for the coring locations, Schmidt Hammer data were taken with an L-type Hammer. This rebound value data was recorded as a proxy for compressive strength of the rock. On the rock the sample was taken from, the smoothest location possible was chosen, and 10 Sharpie dots were drawn on to plan for where the hammer would be used. Then, the hammer was oriented perpendicular to the rock surface and gently pushed against the rock until the spring bounced back and the hammer recorded a Q value. All 10 compressive strength proxies were recorded, as well as the mean and the standard deviation of each set, as provided by the hammer. According to Dr. Surpless, because of the frequency of anomalies in the rock surface, a more accurate way to measure the compressive strength of a rock is to take the maximum value instead of the average. So, the highest rebound value of each sample location will be used in this paper. Schmidt Hammer data was not obtained at BS18-C1, C2, and C3 locations because the coring was done at the same time that the hammer was being used on the other side of the canyon.

Compressive strength was not possible to record at the location for BS18-10 and 11 because the rock crumbled readily under too hard of a touch.

Petrographic Data

Hand samples from various locations in the canyon and stratigraphy were taken while in the field. The samples were made into thin sections by a third party. While examining the thin sections, Table 1 was used to gather observations. Microscopes with both plain polarized light (PPL) and cross polarized light (XPL) were used, as well as the photo tool called "Spot". When taking photos of the thin sections, three locations around the section were chosen. All photos in each section were taken with the stage at the same rotation so that all fractures identified in each photo could be compared to the other photos for the same section. Once a photo was taken, a scale bar was added within the same program. Microfractures in the sections were outlined to potentially observe a pattern in orientations.

Stereonets

At labs at Trinity and Wooster, Allmendinger's Stereonet software was used to visualize fracture orientations. Stereonets are used to represent 3D planar data in a simplified 2D way. Fracture data were organized and made into .csv files, brought into Stereonet, and plotted from there. The stereographic projections were analyzed to find patterns, aiding the analysis of the fracture orientations that were collected in the form of number tables, as seen in Appendix A. Strike and dip averages were calculated using excel, not taking dip direction into account when determining the dip averages due to the uncertainty of the validity of the recorded dip direction.

Sample	
Minerals, dominant Minerals, trace	
Grain size Sorting Roundness Sphericity	Very coarse Coarse Medium Fine Very Fine Poorly Moderately Well Angular Subangular Subrounded Rounded Low High
Compositional maturity Textural maturity	Immature Submature Mature Supermature Immature Submature Mature Supermature
Grain contacts	Point Planar Concavo/Convex Suture
Cement	Calcite Iron Oxide Quartz Epoxy
Deformation features	

Table 1: Classifications used for thin sections when examined under microscope.

Results

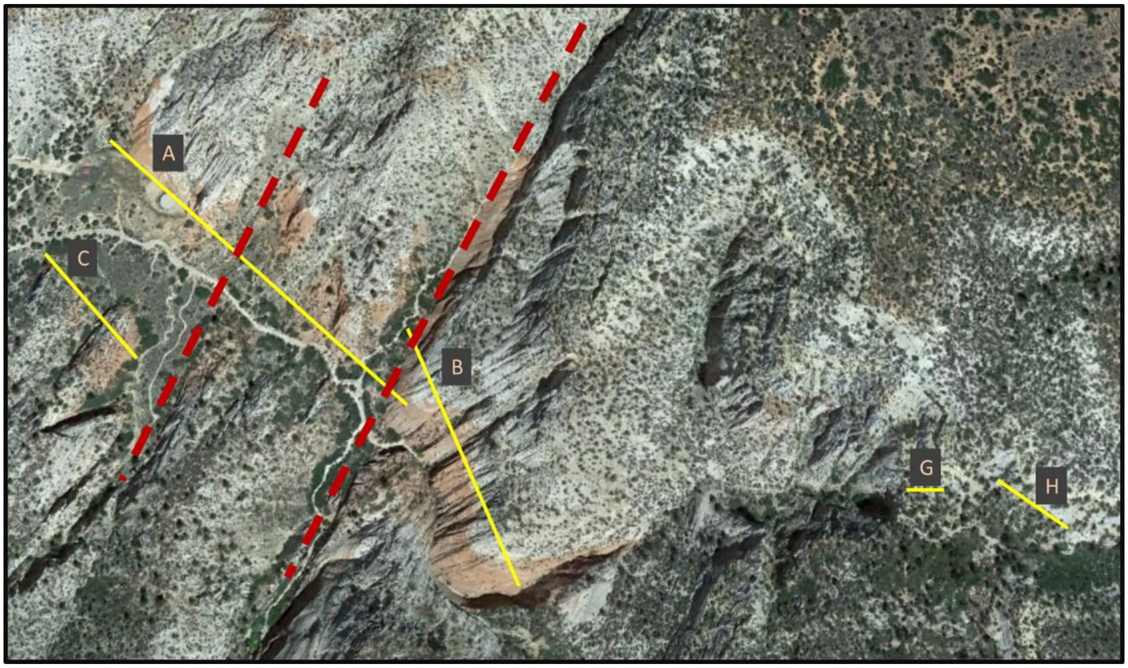

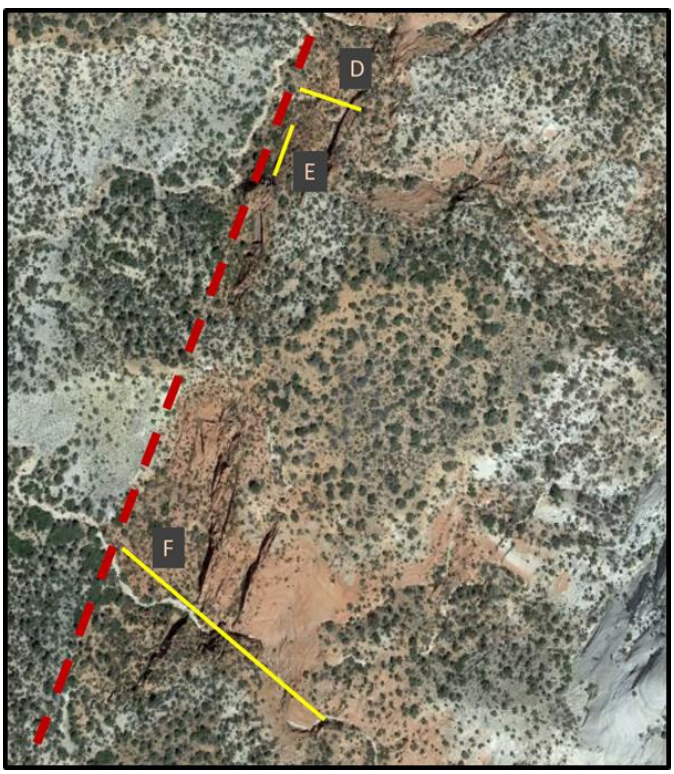

Figure 4 (above): Satellite imagery with Red Hollow Canyon scanlines drawn in yellow. Mountain Lion Den and Kimbler Faults represented by red dashed lines.

Figure 5 (left): Satellite imagery with Elkheart Cliffs scanlines drawn in yellow. Elkheart Cliffs Fault represented by red dashed line.

Figures 4 and 5 show where the scanline data for this study were collected. Five scanlines are in Red Hollow Canyon and three are in the Elkheart Cliffs area. GPS coordinates were recorded at the beginning of each scanline, as seen in Table 2. Field notes for the scanlines can be found in Appendix A and simplified fracture data in Appendix B.

Beginning of scanline:	GPS coordinates			Number of fractures
	Meters N	Meters E	Elevation	
A	4126006.46	355912.95	1746.32	102
B	4125832.42	356347.01	1765.92	81
C	4125799.80	355823.95	1756.05	47
D	4124350.55	355196.37	1734.55	31
E	4124262.84	355141.52	1707.54	18
F	4123877.73	355204.04	1752.03	39
G	4125496.03	356906.74	1961.89	24
H	4125459.90	357123.11	1966.10	33

Table 2: GPS coordinates recorded at the beginning of scanlines and the amount of fractures recorded in each.

Fracture Data: Red Hollow Canyon

Scanline A

Scanline A is the scanline with the most fractures. It is also the longest and begins the furthest north. The average strike for all 102 fractures in scanline A is 020. Determined purely numerically, the dips on this scanline average at 88°. Fractures 1 through 100 are on the west side of the Mountain Lion Den Fault that runs through Red Hollow Canyon, and 101 and 102 (Figure 6F) are on the east side. Fractures 101 and 102 have strikes very similar to the overall scanline A strike average (023, 65NW and 031, 65NW respectively) but their dips vary from the majority of the rest of the scanline. For the most part, the strikes range from 000 to 040, with a few outliers on either side, but the dips vary from 60° to 90° with an outlier at 48°.

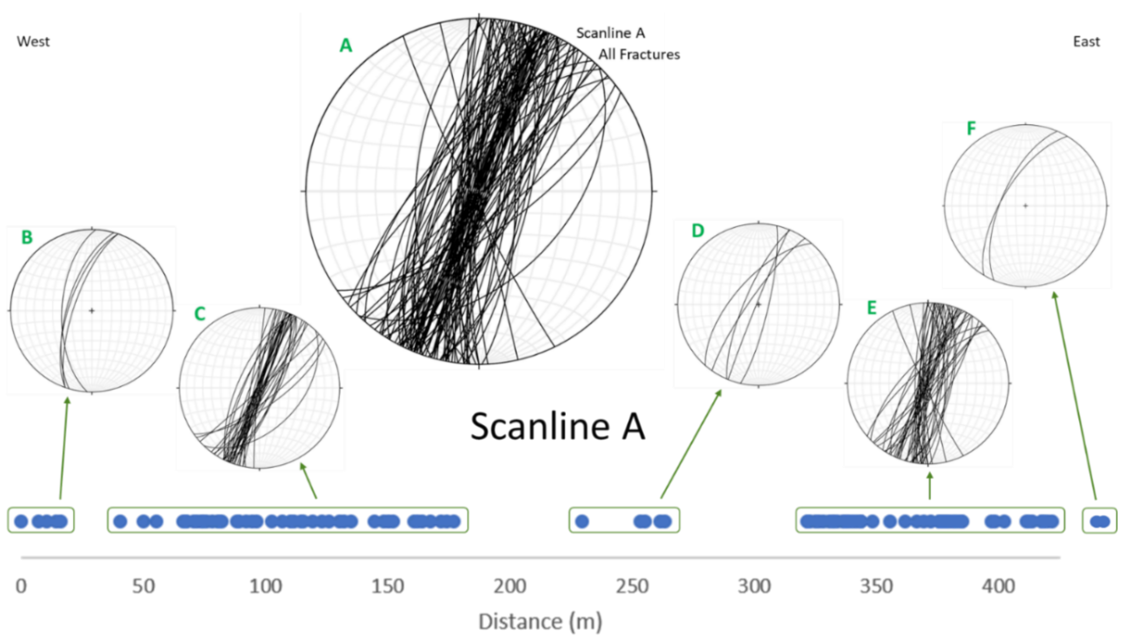

Figure 6 A-F: Stereonets of scanline A and its divisions. (A) All typical fractures in the scanline; (B) furthest west fractures; (C) second fracture grouping; (D) middle grouping; (E) last fracture grouping on west side of MLD Fault; (F) fractures 101 and 102, east of MLD Fault.

Scanline B

Scanline B is the second scanline recorded in the field, started because of a noticeable change in fracture orientation after we crossed the Mountain Lion Den Fault. The average strike for all 66 typical fractures and an unnumbered fracture in scanline B is 054 and the average strike of the 14 diamond fractures is 027, with numerical dip averages of 88° and 81° respectively. As seen in Figure 7A, the fractures in scanline B differ in strike from the fractures in scanline A. The typical fracture strikes along scanline B range from 035 to 085, and the diamond fractures range from 010 to 050, with an outlier at 336. The dips of the typical fractures range from 68° to 90°, with 91% of the dips being greater than or equal to 75°. Dips for the diamond fractures are between 65° and 89°, with an outlier at 50°.

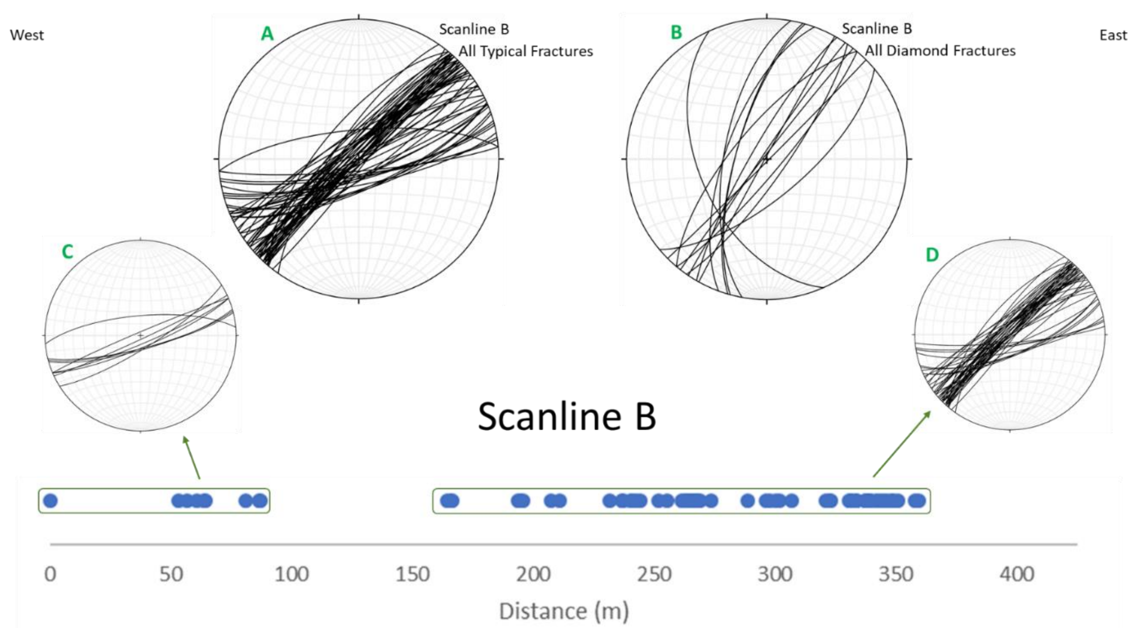

Figure 7 A-D: Stereonets of scanline B and its divisions. (A) All typical fractures in scanline B; (B) diamond fractures; (C) the western grouping; and (D) the eastern grouping.

Scanline C

Scanline C is on the southern side of the canyon and started the furthest west. Of the scanlines in the topographically lower portion of Red Hollow Canyon, this scanline is the shortest and has the least fractures. The average strike for the 30 typical fractures in scanline C is 030 with a numerical dip average of 84° and the average strike of the 17 diamond fractures is 025 with a numerical dip of 75°. The strikes of the typical fractures range from 021 to 045 with outliers at 065 and 359. The typical dips vary from 49° to 88°. Diamond fractures strikes range from 021 to 060 with outliers at 306, 325, 351, 355, and 085. The diamond fractures dip between 51° and 90°, with an outlier at 38°.

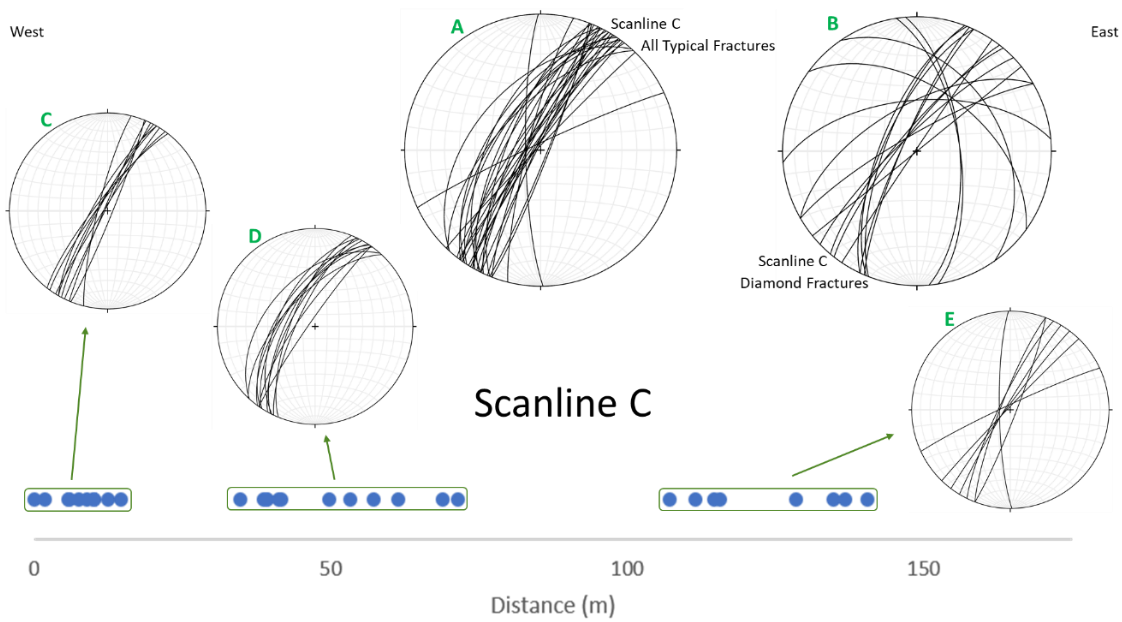

Figure 8 A-E: Stereonets of scanline C and its divisions. (A) All typical fractures in scanline C; (B) diamond fractures; (C) the western grouping; (D) the middle grouping; (E) the eastern grouping.

Scanline G

Scanline G is in the topographically higher, eastern portion of Red Hollow Canyon. The scanline was started just east of the cliff at a heavily fractured zone. The average strike for all 24 fractures on the scanline is 032 with a numerical dip of 79°. The strikes along scanline G range from 022 to 066, with two outliers with strikes of 290 and 325. The dips of fractures range from 65° to 89°, with an outlier with a dip of 54°. A little more than 80% of the dips in the scanline are greater than 75°.

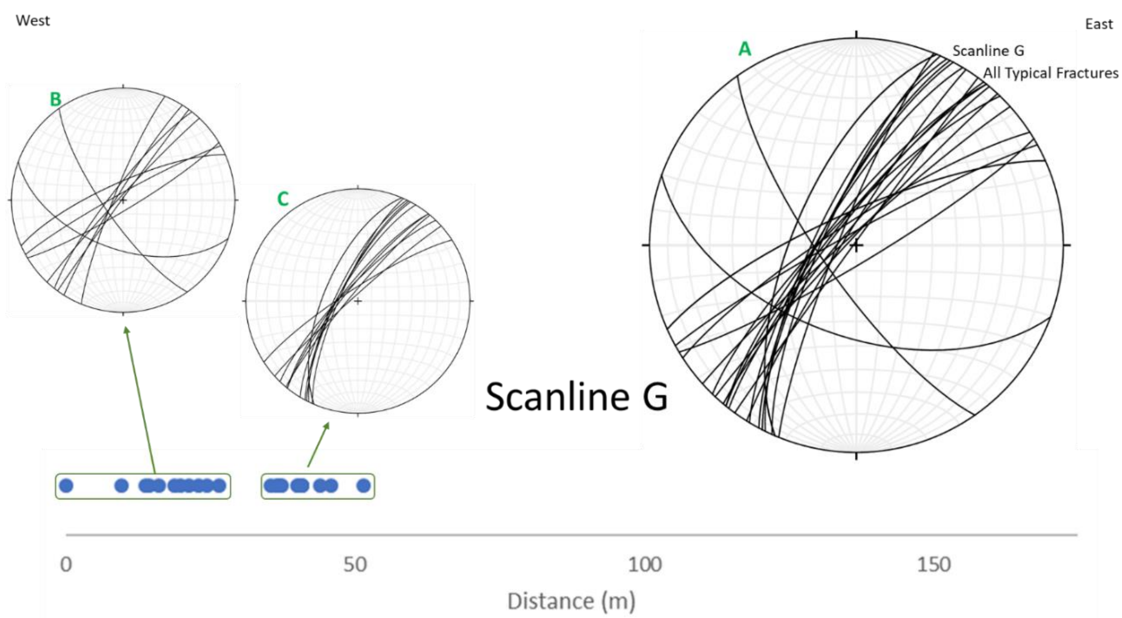

Figure 9 A-C: Stereonets of scanline G and its divisions. (A) All fractures in scanline G; (B) the western grouping; (D) the eastern grouping.

Scanline H

Scanline H is the second recorded scanline in the eastern portion of Red Hollow Canyon, just east of scanline G. Scanline H is the furthest east of all the scanlines and likely the furthest away from a major fault. The average strike of the 31 typical fractures is 037, with a numerical dip average of 85°. The typical strikes along scanline H range from 018 to 054, the diamond fractures have orientations of 038, 67SE and 305, 60SW. Dips of the typical fractures range from 60° to 90°. About 90% of the dips in the scanline are greater than 75°.

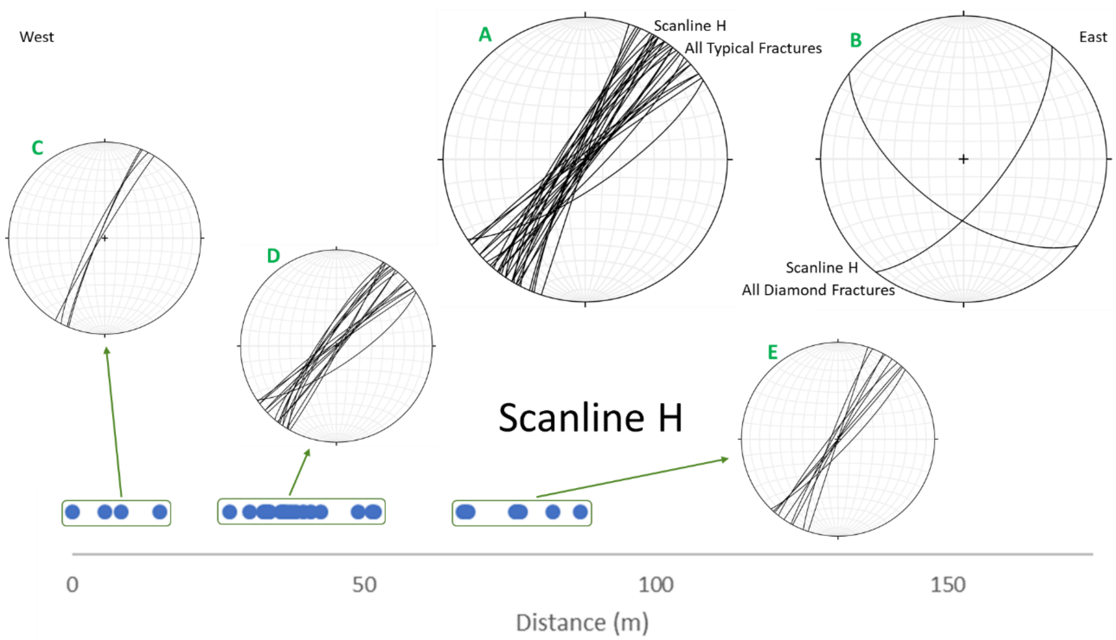

Figure 10 A-E: Stereonets of scanline H and its divisions. (A) All typical fractures in scanline H; (B) both diamond fractures; (C) the western grouping; (D) the middle grouping; (E) the eastern grouping.

Fracture Data: Elkheart Cliffs

Scanline D

Scanline D was the first scanline recorded in Elkheart Cliffs and is just east of the Elkheart Cliffs Fault. The fracture attitudes were taken moving east to west. The average strike for the 31 fractures is 021 with a numerical dip average of 74°. Scanline D fracture strikes vary from 007 to 032 with an outlier at 047. About 25% of the strikes are between 000 and 015. The dip varies from 61° to 87° and roughly half of the dips are 75° or greater.

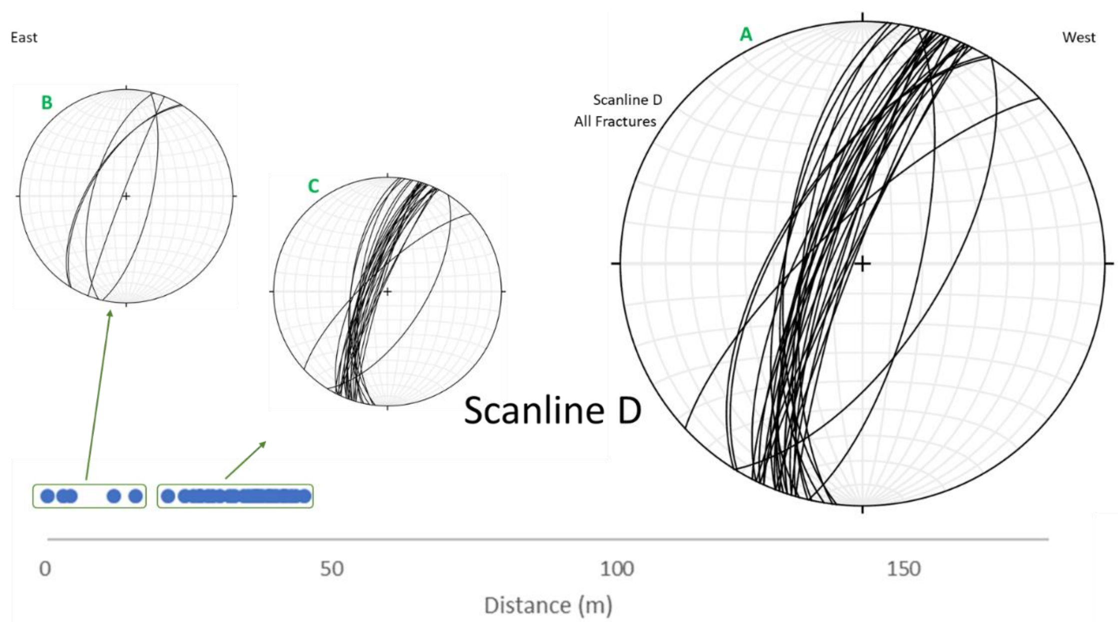

Figure 11 A-C: Stereonets of scanline D and its divisions. Data were taken east to west. (A) All fractures in scanline D; (B) the eastern grouping; (C) the western grouping.

Scanline E

Scanline E was the second scanline in Elkheart Cliffs to be recorded and likely runs parallel to the Elkheart Cliffs Fault. The 14 typical fractures have an average strike of 019 with a numerical dip average of 82°. Strikes of the typical fractures range from 008 to 026, with most of them between 020 and 026. The typical fracture dips vary from 65° to 90°, the 65° one being an outlier by 7°. An estimated 80% of the dips are greater than 75°. The 4 diamond fractures average a 348 strike; however, three of them strike within two degrees of each other , with an outlier at 001.

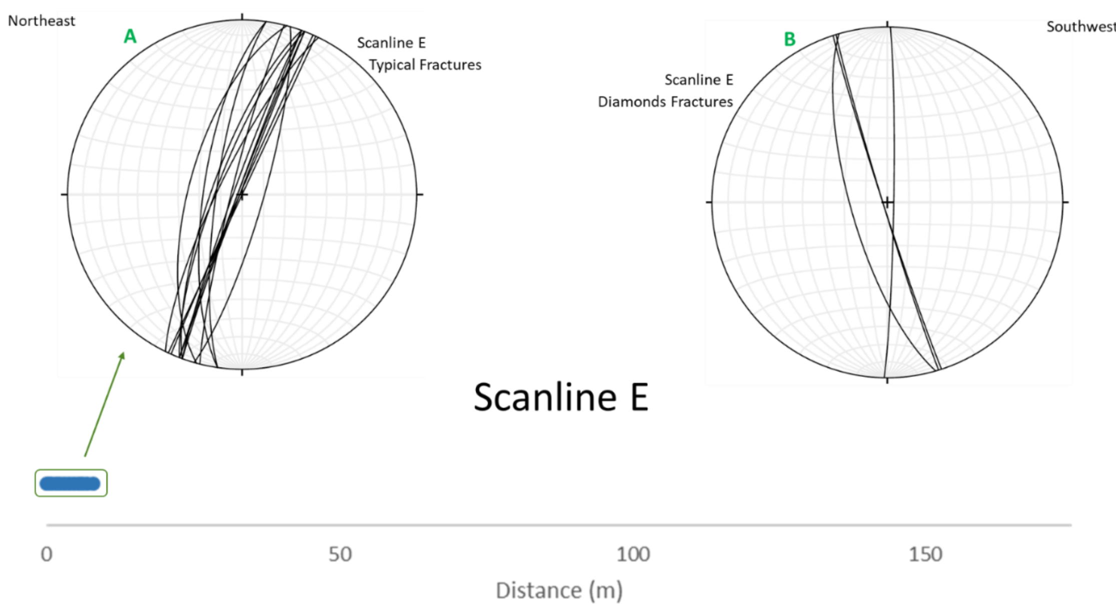

Figure 12 A and B: Stereonets of scanline E and its divisions. (A) All typical fractures in the scanline and (B) all diamond fractures.

Scanline F

Scanline F was the furthest south that data were collected, again moving from east to west. This scanline is east of the Elkheart Cliffs Fault and terminates against it. The average strike of the 39 fractures is 010 with a numerical dip average of 82°. The fractures vary from 353 to 029, with outliers at 042, 336, and 338. Dips range from 69° to 90°, and 87% of the dips are 75° or greater.

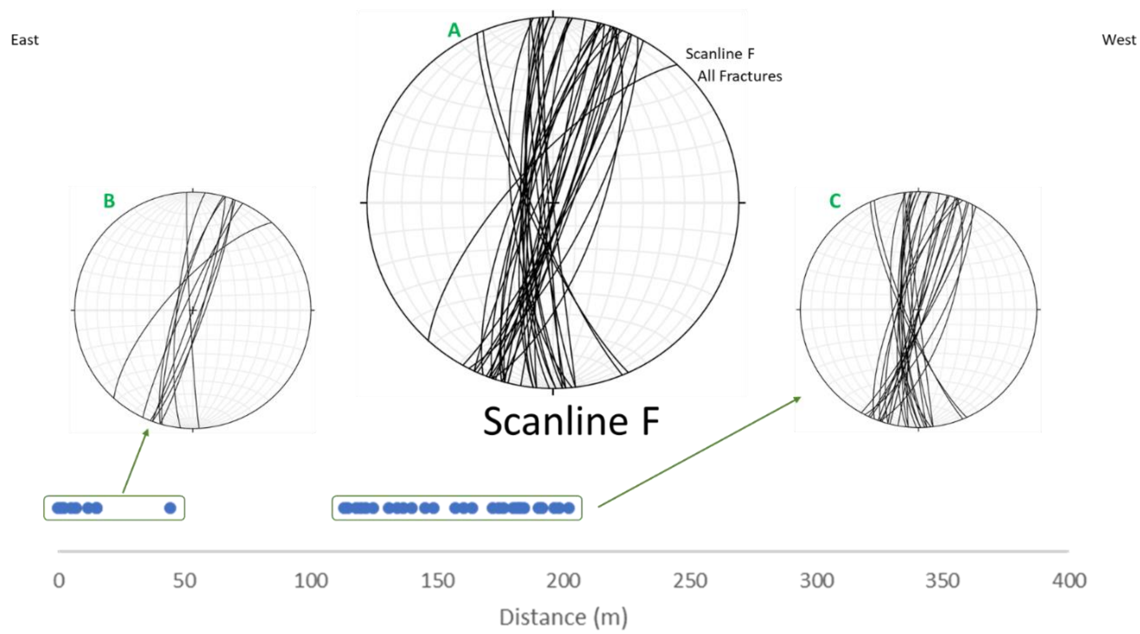

Figure 13 A-C: Stereonets of scanline F and its divisions. Data were taken east to west. (A) All fractures in the scanline; (B) the eastern grouping; (C) the western grouping.

Schmidt Hammer Data

Schmidt Hammer rebound value data in the form of rock compressive strengths were collected from the sites seen in Figure 14. In Red Hollow Canyon, both a lower, oxidized portion and an upper, bleached portion of the Navajo Sandstone were visible and mostly accessible. Two samples were collected from the oxidized zone and the rest were taken from the bleached zone, all from within Red Hollow Canyon. No data were obtained at the core locations or the heavily bleached part of the Navajo Sandstone. All Schmidt data collected could have been altered due to human error such as picking uneven surfaces for each location, subperpendicular angles of use, and different students collecting data at different locations.

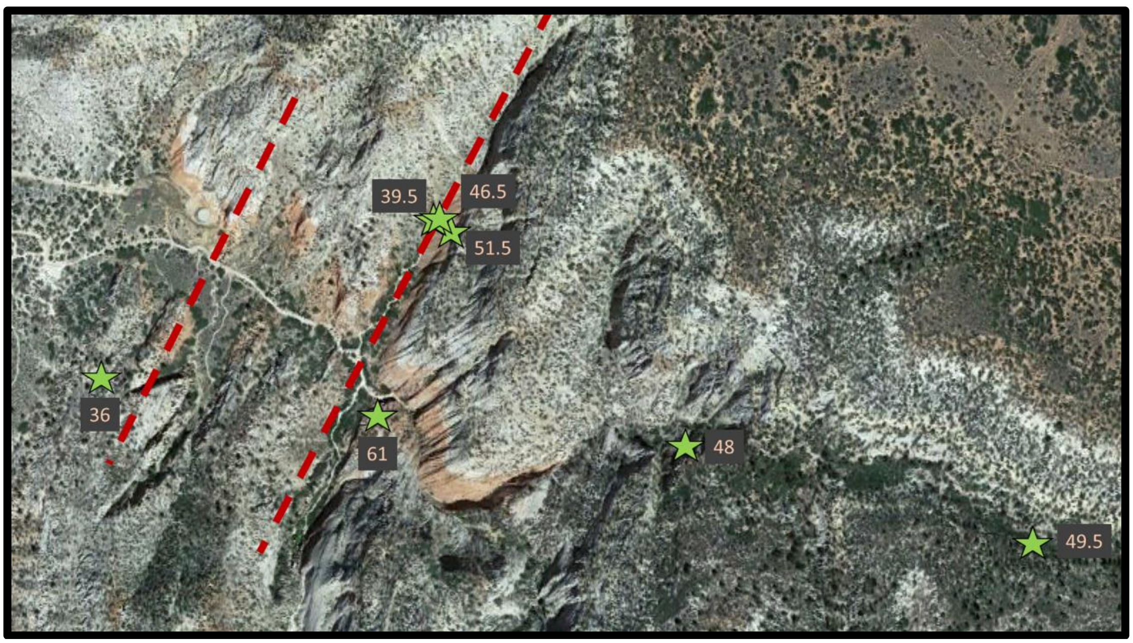

Figure 14: Satellite imagery with sample localities in Red Hollow Canyon tested with the Schmidt Hammer labeled with green stars. Numbers are the maximum rebound values and the red lines represent the Mountain Lion Den and Kimbler Faults ("Google Earth Pro v. 7.3.2, imagery 7/22/2015, 2019 Google").

Schmidt Hammer Data				
Unit	Sample	Maximum	Mean	Standard Deviation
Lower Oxidized	J_{NO}-1$_L$	61	55.7	3.2
Lower Bleached	J_{NB}-2$_L$	39.5	37.2	2.5
Lower Bleached	J_{NB}-3$_L$	46.5	40.5	4.7
Upper Oxidized	J_{NO}-4$_U$	51.5	47.3	2.1
Upper Bleached	J_{NB}-5$_U$	49.5	34.8	8.2
Middle Bleached	J_{NB}-6$_M$	48	40.6	9.5
Middle Bleached	J_{NB}-9$_M$	36	31.8	3.8

Table 3: Schmidt Hammer data (maximums, means, and standard deviations of rebound values) at sample locations in the Navajo Sandstone.

Sample number	Closest fault	Meters to closest fault	Maximum Rebound Value
BS18-J_{NO}-1$_L$	Mountain Lion Den	66.2	61
BS18-J_{NB}-2$_L$	Mountain Lion Den	16.8	39.5
BS18-J_{NB}-3$_L$	Mountain Lion Den	18.3	46.5
BS18-J_{NO}-4$_U$	Mountain Lion Den	23.8	51.5
BS18-J_{NB}-5$_U$	heavily fractured zone	961	49.5
BS18-J_{NB}-6$_M$	heavily fractured zone	228.7	48
BS18-J_{NB}-9$_M$	Elkheart Cliffs	115	36
BS18-J_{NB}-9$_M$	Kimbler	218.3	36
BS18-J_{NB}-10	Elkheart Cliffs	0 to 10.7	0
BS18-J_{NB}-11	Elkheart Cliffs	0 to 8.8	0

Table 4: Schmidt Hammer data and estimated sample distance to closest deformed area.

Petrographic Data

All thin sections contain 90% or more quartz, but they vary in both compositional and textural maturity. The grains mostly touch by planar or point contacts. Iron oxides are the common cement when applicable. Every sample shows evidence of stress in the form of microfractures. Grain size is medium to very fine sand and sorting varies widely between thin sections. No gravel or silt sized grains were observed. Thin sections in both PPL and XPL are shown in Appendix D along with the observation charts. No distinguishable pattern in microfractures was observed.

Discussion

Fault-related Fractures

Several trends are apparent in the scanline fracture data shown in Table 5. Numerically averaged dips for all fractures except those on H◇ are within 14° of each other. Strike averages for scanlines A, B◇, C, C◇, D, E, and G only differ by 18°, ranging from 019 to 037. The Mountain Lion Den Fault strikes at 030, the Kimbler Fault at 025, and the Elkheart Cliffs Fault at 020 (Schiefelbein, 2002; Doelling, 2008), which are all very close to the above listed fracture strike averages. Fractures that form at tips of faults tend to be parallel or subparallel to the fault strike and form first, creating a weak zone for the fault to propagate through (McGrath and Davison, 1995; Kattenhorn et al., 2000). Strike averages from near the Mountain Lion Den Fault tend to be close to the fault strike and the same holds true for the Elkheart Cliffs region, supporting the hypothesis that the faults and fractures are related. The similarity between these faults and fractures implies a close chronological relationship, that the fractures around the Mountain Lion Den, Kimbler, and Elkheart Cliffs Faults formed shortly before the faults did, creating paths of least resistance in which the faults could form.

Scanline	Number of Fractures	Typical Fractures Average		Diamond Fractures Average	
		Strike	Dip	Strike	Dip
A	102	020	88	-	-
B	81	054	88	027	81
C	47	030	84	025	75
D	31	021	74	-	-
E	18	019	82	348	84
F	39	010	82	-	-
G	24	032	79	-	-
H	33	037	85	352.5	63.5

Table 5: Average strikes and numerical dip averages for typical and diamond fracture divisions.

Isolated Fractures

Not all the fracture data trend NNE; scanline divisions E◇ and H◇ have strike averages that trend NNW. Rogers et al. (2004) analyzed fractures in Zion National Park and found three main sets that trend NNE, NNW, and NW in chronological order from oldest to youngest. Since the park is geographically close to Red Hollow Canyon, there may be connections between the structures seen in both locations. My datasets show supporting strike orientations for the older two of Rogers et al.'s (2004) sets, however, mostly NNE trending fractures were seen in Red Hollow Canyon rather than their dominantly NNW fractures. Since Rogers et al. (2004) were able to find timing relations between their observed fracture sets, they concluded that the regional stress regime rotated from NNE to NW over time.

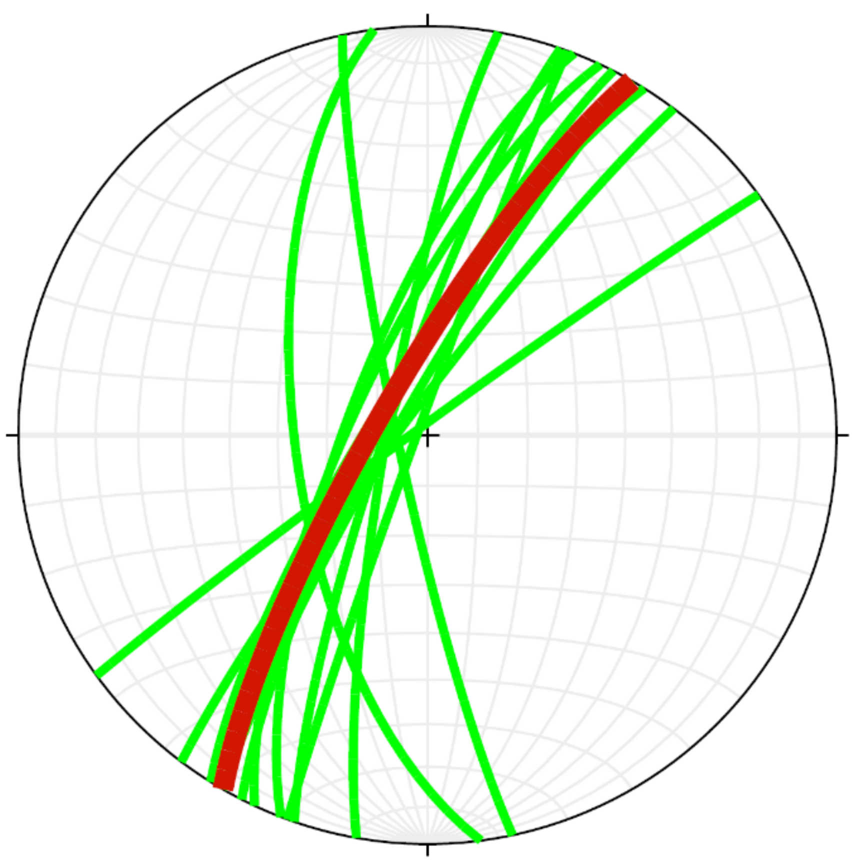

Figure 15: Stereonet showing all typical and diamond fracture division averages from all scanlines in green and the Mountain Lion Den Fault strike in red.

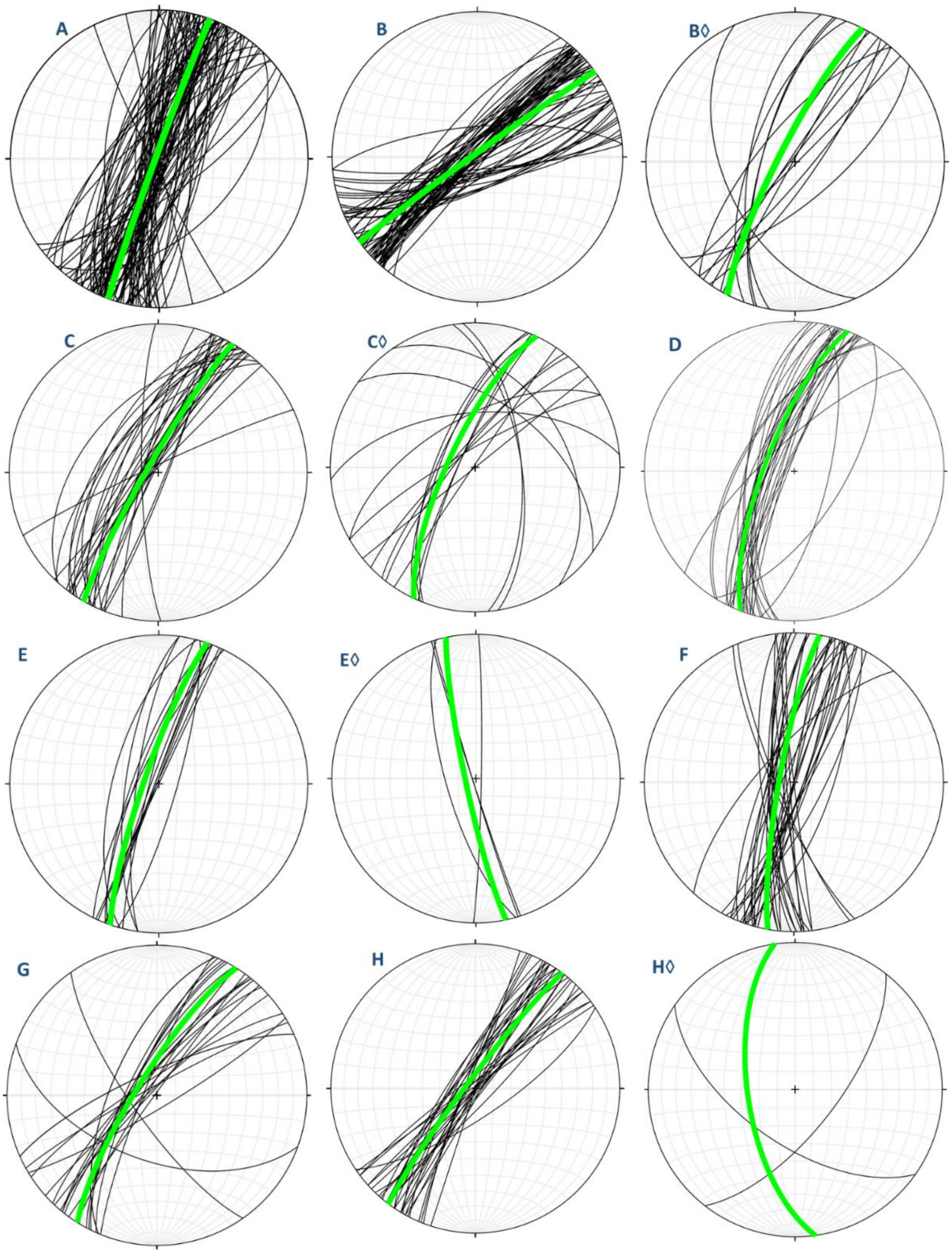

Figure 16 A-H◊: Stereonets of all typical and diamond fracture divisions with their averages in green.

Regional Stress Regime

The average of the fault strikes and the majority of the fracture strike averages is closest to the strike of the Kimbler Fault, so its strike of 025 will be used as a generalized strike for the region. For idealized Andersonian normal faults, σ1 is perpendicular to the surface of the earth and σ3 is in the direction of extension, seen in Figure 17. This means σ3 is ideally perpendicular to the fault strike (Peacock, 2002). As Kattenhorn et al. (2000) found, fractures of similar age to a nearby normal fault will be parallel to sub-parallel to the fault strike and perpendicular to σ1. So, if a fault strikes at 025, then the trend of σ3 would be at 295. Thus, a regional σ3 trending WNW was present when the faults and related fractures formed. Rogers et al. (2004) also found a WNW trending σ3 for a fracture set, that then over time changed to WSW and then to a SW trending σ3, indicating a rotation of the regional stress regime. Since we also see a difference in fracture strikes from NNE to NNW, this supports the σ3 regional rotation hypothesis from Rogers et al.'s (2004) study.

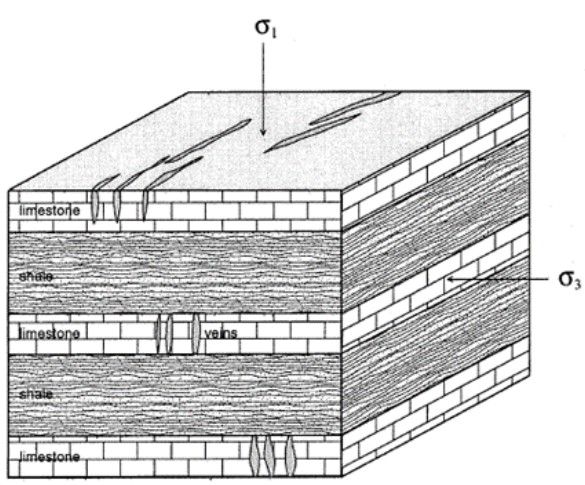

Figure 17: Block diagram showing the maximum (σ1) and minimum (σ3) stress orientations associated with normal faulting and fracturing (Figure 3a from Peacock, 2002).

Fault Propagation

The structural data presented here indicates that the factures in Red Hollow Canyon are close in age to the Mountain Lion Den Fault and associated nearby faults within the Sevier Fault Zone. For the Mountain Lion Den fault, the exact plane where the actual displacement occurred is difficult to define within the canyon due to erosion, landslides, and vegetation, seen in Figure 18. However, displacement of the above Temple Cap Formation is clearly visible on the hanging wall above the eroded area on the north side of the canyon, also seen in Figure 18. Looking south across the canyon, along the approximate fault strike, no offset can be seen. This and the oblique orientation of the fractures to the main fault plane indicate that the fault likely traveled north. Due to the absence of displacement of the Temple Cap Formation on the south side of the canyon, my results suggest that the Mountain Lion Den segment began in Red Hollow Canyon and propagated north.

Northward propagation of the Mountain Lion Den Fault is likely because the Elkheart Cliffs Fault ends just northwest of the canyon, where it has made a relay ramp connecting it to the Highway 89 Fault. The displacement of the Elkheart Cliffs Fault stopped and additional accommodation of offset was necessary, likely initiating the formation of the Mountain Lion Den Fault. However, because the Highway 89 Fault also starts around where the Elkheart Cliffs Fault stops, more research is needed to determine why the displacement was split between the Mountain Lion Den and Highway 89 segments.

Figure 18: Looking north at the approximate Mountain Lion Den Fault strike. Temple Cap Formation sunlit in the background. Left side of the photo is the hanging wall and the right is the footwall. Debris field marking estimated fault strike indicated by the oval (Modified photo BS16_6H. Photo credit: Ben Surpless).

Schmidt Hammer

Maximum rebound values collected in the oxidized zone of the Navajo, at locations of J_{NO}-1_L and J_{NO}-4_U, are the highest. Analysis of rebound values and distances from the sample locations to the closest fault or heavily fractured zone shows no overall correlation, as seen in Table 4. However, the samples from the heavily bleached zone, J_N-10 and J_N-11, located approximately on a fault, were too weak to even get a Schmidt Hammer reading.

Conclusion

In conclusion, I have determined that the Mountain Lion Den Fault originated in Red Hollow Canyon and propagated northward. The chronology of the faults and most fractures in the study area was found to be closely linked; the subparallel fractures likely formed just before the propagation of the fault, allowing for easy propagation.

From this data, we can conclude that:

- Most fractures in Red Hollow Canyon and Elkheart Cliffs are related to the Mountain Lion Den, Kimbler, and Elkheart Cliffs Faults.
- The fault-related fractures are close in age to the fault(s) with which they are associated.
- Data from this study supports Rogers et al.'s (2004) stress regime rotation theory.
- The Mountain Lion Den Fault began in Red Hollow Canyon and propagated north.
- Rebound values taken from the oxidized zone of the Navajo Sandstone are higher than those from the bleached zone.

Studies of additional complex normal faulting regions would help confirm or deny this study. To continue this research, more data could be collected along the Mountain Lion Den Fault, following it north. Also, collecting more fracture data along the Elkheart Cliffs Fault, Kimbler Fault, and the heavily fractured zone east of this study's location would provide valuable insight into how stress was accommodated in this complexly faulted region.

References

Allmendinger, R.W. Stereonet 10 | Rick Allmendinger's Stuff, http://www.geo.cornell.edu/geology/faculty/RWA/programs/stereonet.html (accessed October 2018).

Chidsey, T.C., Jr., Dehamer, J.S., Hartwick, E.E., Johnson, K.R., Schelling, D.D., Sprinkel, D.A., Strickland, D.K., Vrona, J.P., and Wavrek, D.A., 2007, Petroleum geology of Covenant oil field, central Utah thrust belt: Utah Geological Association Publication, v. 36, p. 273–296.

Davis, G.H., 1999, Structural Geology of the Colorado Plateau Region of Southern Utah, with Special Emphasis on Deformation Bands: Geological Society of America, 170 p.

Doelling, H.H., 2008, Geologic map of the Kanab 30'x60' quadrangle: Kane and Washington counties, Utah, and Coconino and Mohave counties, Arizona: Utah Geological Survey Miscellaneous Publications 08-2DM.

Eaton, G.P., 1982, The Basin and Range Province: Origin and Tectonic Significance: Annual Review of Earth and Planetary Sciences, v. 10, p. 409–440, doi:10.1146/annurev.ea.10.050182.002205.

Faulds, J.E., and Varga, R.J., 1998, The role of accommodation zones and transfer zones in the regional segmentation of extended terranes, *in* Faulds, J.E. and Stewart, J.H. eds., Accommodation zones and transfer zones; the regional segmentation of the Basin and Range Province, Geological Society of America, Geological Society of America Special Paper 323.

Fossen, H., 2010, Deformation bands formed during soft-sediment deformation: Observations from SE Utah: Marine and Petroleum Geology, v. 27, p. 215–222, doi:10.1016/j.marpetgeo.2009.06.005.

Fossen, H., and Bale, A., 2007, Deformation bands and their influence on fluid flow: AAPG Bulletin, v. 91, p. 1685–1700, doi:10.1306/07300706146.

Fossen, H., Schultz, R.A., and Torabi, A., 2011, Conditions and implications for compaction band formation in the Navajo Sandstone, Utah: Journal of Structural Geology, v. 33, p. 1477–1490, doi:10.1016/j.jsg.2011.08.001.

Google Earth Pro v. 7.3.2, imagery 7/22/2015, Orderville, Kane County, Utah: 2019 Google, www.earth.google.com.

Jackson, G., 1990a, Tectonic Geomorphology of the Toroweap Fault, western Grand Canyon, Arizona: Implications for Transgression of Faulting on the Colorado Plateau: Arizona Geological Survey: Tucson, AZ, United States.

Jackson, G.W., 1990b, The Toroweap Fault; one of the most active faults in Arizona: Arizona Geological Survey: Tucson, AZ, United States, p. 7–10.

Kattenhorn, S.A., Aydin, A., and Pollard, D.D., 2000, Joints at high angles to normal fault strike: an explanation using 3-D numerical models of fault-perturbed stress fields: Journal of Structural Geology, v. 22, p. 1–23, doi:10.1016/S0191-8141(99)00130-3.

Keck Geology Consortium, 2018, Homepage: Keck Geology Consortium, https://keckgeology.org/ (accessed April 2018).

McGrath, A.G., and Davison, I., 1995, Damage zone geometry around fault tips: Journal of Structural Geology, v. 17, p. 1011–1024, doi:10.1016/0191-8141(94)00116-H.

Moores, E.M., and Twiss, R.J., 1995, Tectonics: New York, W.H. Freeman & Co, 415 p.

Orderville, Utah, 2018, Wikipedia, https://en.wikipedia.org/w/index.php?title=Orderville,_Utah&oldid=844708022.

Peacock, D.C.P., 2002, Propagation, interaction and linkage in normal fault systems: Earth-Science Reviews, v. 58, p. 121–142.

Peterson, F., and Pipiringos, G.N., 1979, Stratigraphic relations of the Navajo Sandstone to Middle Jurassic formations, southern Utah and northern Arizona: U.S. Govt. Print. Off., Professional Paper USGS Numbered Series 1035–B, http://pubs.er.usgs.gov/publication/pp1035B.

Porter, R., Hoisch, T., and Holt, W.E., 2017, The role of lower-crustal hydration in the tectonic evolution of the Colorado Plateau: Tectonophysics, v. 712–713, p. 221–231.

Rogers, C.M., Myers, D.A., and Engelder, T., 2004, Kinematic implications of joint zones and isolated joints in the Navajo Sandstone at Zion National Park, Utah: Evidence for Cordilleran relaxation: Tectonics, v. 23, doi:10.1029/2001TC001329.

Schiefelbein, I.M., 2002, Fault segmentation, fault linkage, and hazards along the Sevier fault, southwestern Utah: University of Nevada, 132 p.

Stewart, J.H., 1998, Regional characteristics, tilt domains, and extensional history of the late Cenozoic Basin and Range Province, western North America, *in* Faulds, J.E. and Stewart, J.H. eds., Accommodation zones and transfer zones; the regional segmentation of the Basin and Range Province, Geological Society of America Special Paper 323.

Surpless, B., 2018, Project Proposal: Structural evolution of a segmented normal fault transfer zone, Sevier Fault, southern Utah, Personal Communication.

Surpless, B., 2017, Structural evolution of a normal fault transfer zone: Keck Geology Consortium, https://keckgeology.org/2017/12/southern-utah/.

Appendix A: Scanline Fracture Data

SCANLINE A: Red Hollow Canyon						
Date	**Fracture Number**	**Dip Direction**	**Dip**	**Position (m)**	**Spacing relative to previous fracture (m)**	**Comment**
18-06-18	1	289	72	0.00	7.26	Right stepping en echelon (observed over 2 meters with mm-cm offset)
	2	N/A	N/A	7.26	5.35	Not accessible
	3	289	67	10.70	3.42	Bends along strike to south to fracture 4 *photos taken on 6/19 show offset
	4	273	60	14.10	2.70	Merges with 5 to south (similar to 3/4 relationship) *photos taken on 6/19 show offset

5	286	65	16.10	13.35	Estimate based on view to North based on 4/5 relationship * photos taken on 6/19 show offset
6	284	85	40.80	17.13	Planar but dies out upward and curves east
7	291	81	50.36	7.23	Splits into 1.5 meter splay to the east
8	282	87	55.26	7.95	Photo with Caroline for scale; splits into multiple splays to south (or merges to north)
9	113	74	66.26	6.14	Left stepping en echelon splays bend toward adjacent fractures' orientation (about 10 cm offset observed). Thin mm deformation band. Madison for scale.

10	127	86	67.53	0.74	Parallel to 11, see fieldbook 2 for sketch
11	127	86	67.75	1.49	Parallel to 10
12	122	82	70.50	2.24	Up slope strike changes from NNE to NNW
13	294	68	72.23	1.71	Dip varies
14	274	88	73.91	1.20	Down slope strike changes from N to NNE
15	125	78	74.62	1.07	mm scale deformation band
16	138	89	76.04	1.89	
17	117	78	78.39	2.39	
18	293	75	80.81	1.45	
19	291	81	81.29	0.53	
20	280	81	81.87	3.45	down slope dip varies (more vertical)
21	124	88	88.18	3.63	
22	292	87	89.13	1.91	
23	296	74	92.00	2.80	
24	297	87	94.73	2.13	
25	290	87	96.26	4.02	Dip direction varies down slope with splays
26	296	88	102.76	5.40	Curves toward NE up slope as dies out

	27	109	86	107.07	3.84	Surrounded by subparallel fractures
	28	145	70	110.44	2.41	Cross-cut by 29, displaced 0.70 m (apparent offset)
	29	105	90	111.89	2.08	
19-06-18	30	142	76	114.59	1.85	2 meters exposed, dip direction varies
	31	102	88	115.59	2.35	Last segment of left stepping en echelon fracture set (see details in field book 1)
	32	109	85	119.29	3.73	
	33	290	88	123.04	3.25	Left stepping 2-5 cm offset en echelon (see details in field book 1)
	34	293	88	125.79	3.59	Left stepping en echelon
	35	112	87	130.23	3.09	Adjacent to horsetail splay complex
	36	290	90	131.97	2.40	
	37	112	86	135.03	6.31	
	38	112	86	144.59	6.76	
	39	106	90	148.55	2.91	

	40	290	89	150.42	1.96	Displays right and left stepping en echelon
	41	109	86	152.47	5.31	
	42	117	72	161.03	4.97	Dip varies
	43	114	88	162.40	1.56	
	44	134	48	164.15	2.60	
	45	108	89	167.60	3.95	
	46	109	85	172.05	3.23	
	47	112	73	174.05	2.57	
	48	117	84	177.20	22.73	
	N/A	N/A	N/A	219.50	26.13	No intact rock present
	49	293	81	229.45	17.05	
	50	103	80	253.60	13.04	Dip varies, irregular left stepping en echelon
	51	305	81	255.53	4.08	
	52	293	76	261.76	3.93	
	53	311	65	263.38	8.33	
	End of outcrop	N/A	N/A	278.41	29.18	End of outcrop
20-06-18	N/A	N/A	N/A	321.73	21.66	No intact rock present
	54	292	88	321.73	0.32	left-stepping en echelon
	55	244	86	322.37	0.41	left-stepping en echelon
	56	292	84	322.56	1.41	left-stepping en echelon
	57	271	77	325.20	1.86	appears left-stepping and en echelon

58	291	90	326.28	1.50	appears left-stepping and en echelon
59	103	68	328.20	2.20	
60	275	83	330.67	1.98	
61	103	66	332.16	0.97	
62	280	84	332.62	0.98	
63	279	88	334.13	1.82	
64	270	82	336.27	1.34	
65	106	88	336.81	0.75	
66	107	77	337.76	1.05	
67	94	80	338.91	1.19	
68	101	86	340.13	1.39	
69	273	81	341.70	1.71	
70	277	80	343.55	1.05	
71	281	89	343.80	2.36	
72	270	85	348.28	5.81	more vertical upwards at an inaccessible point, dip varies
73	275	89	355.41	6.63	
74	278	85	361.53	5.50	
75	123	70	366.41	4.03	Changes in orientation along strike
76	293	89	369.59	2.91	
77	97	76	372.24	2.93	
78	89	73	375.44	1.89	
79	285	86	376.03	0.59	
80	267	86	376.61	0.83	upslope crossing with fracture #79
81	274	90	377.69	0.91	
82	290	83	378.43	0.69	
83	301	83	379.08	0.69	
84	101	78	379.81	1.24	

	85	133	88	381.56	1.11	
	86	77	90	382.03	0.72	
	87	95	71	383.00	1.30	
	88	295	87	384.62	1.11	
	89	294	90	385.22	6.22	
	90	129	78	397.07	6.57	last accessible fracture before main fault
	91	106	86	398.37	2.63	estimate (Caroline meter ~4ft)
	92	281	82	402.32	6.57	many left-stepping en echelon, curves towards fracture #91
	93	315	67	411.52	5.07	
	94	319	75	412.46	1.23	
	95	132	85	413.98	0.76	
	End of outcrop	N/A	N/A	413.98	1.75	End of outcrop
	96	304	76	417.48	2.05	crossed fault
	97	297	71	418.08	0.56	dip varies
	98	122	81	418.61	1.00	Dip direction varies
	99	118	84	420.07	1.66	
	100	119	90	421.92	0.93	
	101	293	65	N/A	0.60	immediately adjacent to Fracture 6 in scanline B
	102	301	66	N/A		immediately adjacent to Fracture 6 in scanline B

Table 6: Notes from the field on scanline A.

SCANLINE B: Red Hollow Canyon						
New fracture set is at low angle to scanline A. We may relate future fractures to scanline A (depending on orientation)						
Date	**Fracture Number**	**Dip Direction**	**Dip**	**Position (m)**	**Spacing relative to previous fracture (m)**	**Comments**
21-06-18	1	165	79	0.00		started new scanline because of change in fracture orientation
	2	355	73	53.09	53.09	sightline between fractures 1/2 is 206 degrees
	3	148	79	56.69	3.60	
	4	157	83	60.57	3.88	dip varies
	5	164	78	63.66	3.09	
	6	166	79	64.18	0.52	adjacent to scanline A, fractures 101/102
	7	157	80	81.21	17.03	
	8	337	87	86.70	5.49	
	9	155	87	87.22	0.52	
	*	*	*	*	*	*at BS18-15, we stopped documenting scanline B fracture network because more complex, with fractures not consistent with approximate scanline B orientations

◇	246	50		36.08	these fractures are not included in scanline B data
◇	290	66			these fractures are not included in scanline B data
◇	300	81			these fractures are not included in scanline B data
10	169	75	at BS18-16	76.95	
11	172	81	1.85	1.85	
12	175	83	2.17	0.32	
◇	286	72			these fractures are not included in scanline B data
◇	285	72			these fractures are not included in scanline B data
◇	280	65			these fractures are not included in scanline B data
13	171	80	29.52	27.35	
14	156	73	30.40	0.88	
15	161	72	31.32	0.92	
16	158	81	42.90	11.58	
◇	299	89			
17	156	72	46.84	3.94	
◇	140	68			
◇	125	79			
◇	130	82			
◇	135	89			

	◇1	308	88			End of 6/21/2018 (BS18-17)
22-06-18	◇2	304	87		11.76	distance is between ◇1/◇2
	◇	310	71			same fracture as above (◇2), change in dip downward in outcrop (71 degree fracture is at a lower surface than 87 degree fracture)
	18	160	73	20.68	8.92	
	19	146	88	25.48	4.80	
	20	148	90	26.00	0.52	
	21	141	87	29.13	3.13	
	22	137	89	30.18	1.05	
	23	323	82	31.82	1.64	
	24	330	82	33.18	1.36	
	25	137	90	40.52	7.34	sketch in field book 1
	26	333	80	44.03	3.51	
	-	310	68			
	27	312	86	50.14	6.11	
	28	135	90	51.45	1.31	
	29	128	86	52.46	1.01	
	30	312	76	52.99	0.53	
	31	318	87	53.83	0.84	
	32	315	90	54.06	0.23	
	33	136	87	54.26	0.20	
	34	318	85	55.17	0.91	
	35	319	90	55.61	0.44	
	36	143	80	56.81	1.20	significant dip variation
	37	312	84	57.69	0.88	
	38	305	76	62.48	4.79	

39	154	90	77.43	14.95	
40	315	88	85.07	7.64	
41	315	83	86.51	1.44	
42	319	87	89.10	2.59	
43	317	85	90.95	1.85	
44	322	83	95.57	4.62	
45	321	82	110.05	14.48	
46	313	90	111.23	1.18	
47	312	90	112.13	0.90	
48	311	88	119.30	7.17	dip varies upslope of fracture (anastomosing in cross section)
49	313	86	120.19	0.89	(anastomosing in cross section)
50	315	77	120.69	0.50	(anastomosing in cross section)
51	319	90	122.34	1.65	
52	311	84	122.64	0.30	
53	311	90	126.04	3.40	
54	321	83	126.72	0.68	right stepping en echelon in map view
55	313	88	127.56	0.84	
56	311	90	127.91	0.35	
57	310	80	128.30	0.39	
58	313	81	130.43	2.13	
59	316	83	132.09	1.66	
60	329	76	133.70	1.61	
61	322	83	135.29	1.59	
62	322	81	137.08	1.79	
63	321	82	137.58	0.50	
64	135	87	139.49	1.91	
65	311	81	146.54	7.05	

	66	325	75	148.17	1.63	End of accessible scanline B, at BS18-18 we ended scanline B
						Additional scanline B fractures may be added once drone photos have been added

Table 7: Notes from the field on scanline B.

SCANLINE C: Red Hollow Canyon						
Scanline C perpendicular to the dominant fracture set						
Date	**Fracture Number**	**Dip Direction**	**Dip**	**Position (m)**	**Spacing relative to previous fracture (m)**	**Comments**
23-06-18	1◇	295	81	GPS		BS18-19
	2◇	355	59			drastically different fracture orientations
	3◇	330	62			
	4◇	295	70			huge curve, about 90 degree turn to south
	5◇	316	80			huge curve, turns to west; many small fractures with varying orientations
	6◇	330	80			many small fractures crossing perpendicular
	7◇	292	68			left stepping, cm-1/2 meter scale; slight curve; possible deformation band (photos)
	8◇	310	78			
	9◇	293	81			
	10◇	291	71			possibly continues north; top inaccessible
	11◇	321	90			
	12◇	308	80			

13◇	304	89			
1	308	80	0.00		start of scanline C (BS18-20)
14●	55	38			subperpendiular to scanline C
15●	36	51			subperpendiular to scanline C
2	112	86	1.89		
3	284	82	5.81		
4	293	87	5.96		
5	300	78	7.51		
6	298	83	9.01		
7	300	82	10.08		
8	296	88	10.13		
9	306	82	12.53		
10	302	87	14.68		BS18-21 (when Carol/Charley switched with Curtis/Madison
11	303	64	0.00		BS18-22 - starting a new position on the scanline because there was a large gap where no surface was exposed); dip varies
12	305	85	3.97		
13	305	76		0.38	
14	295	75		0.36	
15	297	67		1.85	
16	313	64		0.35	estimated position
16●	81	64			
17	312	49		8.12	left stepping en echelon
18	304	59		3.66	
17●	85	64			
19	292	70		3.98	
20	299	70		4.07	
21	306	63		7.49	

	22	296	59		2.49	
	23	307	87		35.70	
						inaccessible fractures in between 23/24. Position gap ?
	24	269	81		4.36	
	25	111	85		3.22	
	26	291	82		0.93	
	27	314	88		12.87	
	28	335	86		6.28	dip and dip direction varies greatly upslope
	29	296	81		1.94	left stepping en echelon; dip varies slightly upslope
	30	301	86		3.90	

Table 8: Notes from the field on scanline C.

SCANLINE D: Elkheart Cliffs						
Scanline approximately perpendicular to major faults (trending approximately 305 degrees**)						
**scanline orientation between fractures 4/5 is 335 degrees-for remainder of scanline orientation remained 305						
Date	**Fracture Number**	**Dip Direction**	**Dip**	**Position (m)**	**Spacing relative to previous fracture (m)**	**Comments**
24-06-18	1	291	87	0.00		variable dip. Begin scanline D
	2	103	71	2.68		in rubbly zone, likely part of complex fracture system *possible fault/shear fracture
	3	285	64	4.11		dip varies significantly upslope *possible fault/shear fracture
	4	301	62	11.64		*possible fault/shear fracture
	5	302	61		3.85	scanline changes angle, see fieldbook 1: pg. 119 (*possible fault/shear fracture)
	6	122	63		5.67	*possible fault/shear fracture

	7	288	76		2.99	right stepping, see photo in fieldbook 1 *possible fault/shear fracture
	8	291	72		1.33	*possible fault/shear fracture
	9	296	69		1.14	gently left steps, 5-20 cm *possible fault/shear fracture
	10	289	72		0.23	*possible fault/shear fracture
	11	288	71		1.21	
	12	283	73		0.92	
	13	277	70		1.13	
	14	276	64		1.65	
	15	282	71		1.00	
	16	291	76		1.60	
	17	317	75		0.82	
	18	288	76		0.80	
	19	290	74		0.41	
	20	279	64		0.55	
	21	295	74		0.59	
	22	286	79		0.96	
	23	294	80		0.35	
	24	294	77		0.55	
	25	297	77		0.68	
	26	287	83		0.98	
	27	295	86		0.37	
	28	290	82		0.16	20 cm left steps
	29	287	78		0.93	
	30	296	85		0.85	
	31	286	85		1.46	

Table 9: Notes from the field on scanline D.

SCANLINE E: Elkheart Cliffs						
Date	**Fracture Number**	**Dip Direction**	**Dip**	**Position (m)**	**Spacing relative to previous fracture (m)**	**Comments**
24-06-18	1	278	78	0.00		start of scanline E
	2	291	88	0.46		
	3	290	76	0.75		
	4	278	72	1.56		
	5	291	78	2.16		appears to be listric
	◇1	91	87	0.00		also possibly listric, at different orientation…so ? , mm scale deformation band subparallel
	6	106	80	2.95		
	◇2	253	88	0.93		dip varies, possible deformation band mm scale
	7	290	88	3.95		
	◇3	252	88	4.80		
	8	290	86	4.62		
	9	291	89	5.48		
	10	284	85	6.19		dip and orientation varies
	11	296	79	6.99		dip varies, possible turns into ◇4
	◇4	254	73	10.74		
	12	285	65	?		but shallows to 277 degrees, 52 degrees upward (possible step-back in the scanline so position is in question)

	13	294	89	7.88		measured from fracture 11 position
	14	295	90	?		up against fault, position is step-back in scanline

Table 10: Notes from the field on scanline E.

SCANLINE F: Elkheart Cliffs						
Date	**Fracture Number**	**Dip Direction**	**Dip**	**Position (m)**	**Spacing relative to previous fracture (m)**	**Comments**
27-06-18	1	286	78	0.00		start of scanline F; BS18-29; right/left steps seen
	2	110	82	1.00		dip varies upslope, may merge with fracture 1
	3	276	79	1.80		
	4	285	80	2.29		dip varies
	5	106	84	4.93		deformation bands (mm scale)
	6	295	84	6.84		
	7	111	85	11.63		dip varies downslope
	8	267	88	15.17		dip varies slightly
	9	110	90	GPS		BS18-30
	10	312	72	GPS		BS18-31; dip varies significantly, possibly due to erosion
	11	114	84	GPS		BS18-32; spacing narrows upslope
	12	289	77	calc. based on GPS	1.51	dip varies; spacing narrows upslope
	13	110	90		3.62	
	14	119	83		1.70	

15	108	89		1.94	
16	115	84		2.92	
17	292	74		6.24	
18	284	90		3.15	
19	109	85		2.59	possible deformation band/fill - no reaction to HCl
20	109	69		3.09	
21	117	74		5.48	dip and dip direction varies
22	104	90		3.17	dip varies
23	275	85		8.53	left steps (mm-cm scale)
24	263	90		3.61	
25	266	86		3.43	possible (mm scale) deformation band
26	285	87		7.79	possible (mm scale) deformation band
27	248	81		2.69	possible (mm scale) deformation band
28	246	79		1.97	possible (mm scale) deformation band
29	263	84		3.40	possible (mm scale) deformation band
30	266	79		1.72	
31	264	72		0.78	
32	276	77		0.66	
33	269	78		1.19	
34	269	76		5.84	

	35	271	77		0.99	mm scale deformation band
	36	267	79		0.69	mm scale deformation band
	37	275	80		4.39	
	38	100	90		2.11	
	39	285	76		3.65	dip varies; end of scanline

Table 11: Notes from the field on scanline F.

SCANLINE G: Red Hollow Canyon						
parallel to cliff face						
Date	**Fracture Number**	**Dip Direction**	**Dip**	**Position (m)**	**Spacing relative to previous fracture (m)**	**Comments**
28-06-18	1	235	76	0.00		BS18-36; dip varies
	2	149	83	9.61		
	3	336	77	13.81		many small fracture splays
	4	336	77	14.36		dip varies; many small fracture splays
	5	308	81	16.07		right stepping
	6	292	83	18.77		
	7	302	85	19.94		
	8	200	54	21.39		dip varies
	9	313	87	22.88		right and left stepping
	10	331	85	24.34		
	11	306	89	26.44		mm scale calcite fill
	12	310	84	35.48		
	13	309	80	36.57		
	14	318	86	36.73		
	15	314	79	37.14		
	16	327	81	37.31		
	17	301	76	40.14	2.83	merges with 18 downslope
	18	296	74	40.36	0.22	merges with 17 downslope
	19	298	76	40.62	0.26	
	20	309	78	40.78	0.16	

	21	293	65	40.88	0.10	dip steepens up-dip
	22	293	65	40.93	0.05	dip steepens up-dip
	23	297	76	44.11	3.18	mm scale right steps
	24	294	77	45.80	1.69	
	25	N/A	N/A	51.59	5.79	begin complexly fractured area

Table 12: Notes from the field on scanline G.

SCANLINE H: Red Hollow Canyon						
scanline H will run West to East in upper Navajo sandstone and is East of scanline G						
Date	**Fracture Number**	**Dip Direction**	**Dip**	**Position (m)**	**Spacing relative to previous fracture (m)**	**Comments**
28-06-18	1	301	87	0.00		BS18-37; left stepping
	2	293	85	5.62		dip changes upslope
	3	292	85	8.36	2.74	near base of outcrop; six splays (no dominant fracture orientation)
	4	297	80	14.99	6.63	
	◇1	128	67		N/A	multiple fractures subparallel
	5	304	76	27.10	12.11	
	6	146	74	30.47	3.37	merges with 7
	◇2	217	60		N/A	deformation band- no HCl reaction
	7	128	86	32.72	2.25	merges with 6
	8	323	84	33.19	0.47	
	9	300	77	33.39	0.20	
	10	310	80	33.54	0.15	
	11	301	82	33.93	0.39	
	12	323	87	35.88	1.95	
	13	128	87	36.31	0.43	
	14	121	89	36.65	0.34	
	15	318	87	37.42	0.77	

	16	318	90	38.36	0.94	short fracture segments upslope between 16/17
	17	136	89	39.71	1.35	short fracture segments upslope between 16/17
	18	119	87	40.95	1.24	dip varies upslope
	19	304	82	42.63	1.68	
	20	306	79	49.00	6.37	mm scale deformation band
	21	307	80	51.46	2.46	
	22	325	89	51.76	0.30	
	GAP					short segmented fractures
	23	134	81	67.01	15.25	
	24	132	88	67.45	0.44	
	25	124	90	67.95	0.50	
	26	299	86	75.98	8.03	
	27	118	90	76.24	0.26	
	28	291	84	76.46	0.22	
	29	288	90	76.76	0.30	
	30	308	84	82.45	5.69	
	31	311	90	87.05	4.60	

Table 13: Notes from the field on scanline H.

Appendix B: Simplified Scanline Fracture Data

Table 14: Fracture numbers, strikes, and strikes converted to northern hemisphere azimuthal notation.

Scanline A fracture attitudes			Scanline B fracture attitudes		
Fracture Number	**Strike**	**Strike's northerly reading**	**Fracture Number**	**Strike**	**Strike's northerly reading**
1	199	019	1	075	075
2			2	265	085
3	199	019	3	058	058
4	183	003	4	067	067
5	196	016	5	074	074
6	194	014	6	076	076
7	201	021	7	067	067
8	192	012	8	247	067
9	023	023	9	065	065
10	037	037	◇	156	336
11	037	037	◇	200	020
12	032	032	◇	210	030
13	204	024	10	079	079
14	184	004	11	082	082
15	035	035	12	085	085
16	048	048	◇	196	016
17	027	027	◇	195	015
18	203	023	◇	190	010
19	201	021	13	081	081
20	190	010	14	066	066
21	034	034	15	071	071
22	202	022	16	068	068
23	206	026	◇	209	029
24	207	027	17	066	066
25	200	020	◇	050	050
26	206	026	◇	035	035
27	019	019	◇	040	040
28	055	055	◇	045	045
29	015	015	◇1	218	038
30	052	052	◇2	214	034
31	012	012	◇	220	040
32	019	019	18	070	070
33	200	020	19	056	056
34	203	023	20	058	058
35	022	022	21	051	051

36	200	020	22	047	047
37	022	022	23	233	053
38	022	022	24	240	060
39	016	016	25	047	047
40	200	020	26	243	063
41	019	019	-	220	040
42	027	027	27	222	042
43	024	024	28	045	045
44	044	044	29	038	038
45	018	018	30	222	042
46	019	019	31	228	048
47	022	022	32	225	045
48	027	027	33	046	046
49	203	023	34	228	048
50	013	013	35	229	049
51	215	035	36	053	053
52	203	023	37	222	042
53	221	041	38	215	035
End of outcrop			39	064	064
54	202	022	40	225	045
55	154	334	41	225	045
56	202	022	42	229	049
57	181	001	43	227	047
58	201	021	44	232	052
59	013	013	45	231	051
60	185	005	46	223	043
61	013	013	47	222	042
62	190	010	48	221	041
63	189	009	49	223	043
64	180	00	50	225	045
65	016	016	51	229	049
66	017	017	52	221	041
67	004	004	53	221	041
68	011	011	54	231	051
69	183	003	55	223	043
70	187	007	56	221	041
71	191	011	57	220	040
72	180	00	58	223	043
73	185	005	59	226	046
74	188	008	60	239	059
75	033	033	61	232	052
76	203	023	62	232	052
77	007	007	63	231	051
78	359	359	64	045	045

79	195	015	65	221	041
80	177	357	66	235	055
81	184	004			
82	200	020			
83	211	031			
84	011	011			
85	043	043			
86	347	347			
87	005	005			
88	205	025			
89	204	024			
90	039	039			
91	016	016			
92	191	011			
93	225	045			
94	229	049			
95	042	042			
End of outcrop					
96	214	034			
97	207	027			
98	032	032			
99	028	028			
100	029	029			
101	203	023			
102	211	031			

Scanline C fracture attitudes			Scanline D fracture attitudes		
Fracture Number	**Strike**	**Strike's northerly reading**	**Fracture Number**	**Strike**	**Strike's northerly reading**
1◇	205	025	1	201	021
2◇	265	085	2	013	013
3◇	240	060	3	195	015
4◇	205	025	4	211	031
5◇	226	046	5	212	032
6◇	240	060	6	032	032
7◇	202	022	7	198	018
8◇	220	040	8	201	021
9◇	203	023	9	206	026
10◇	201	021	10	199	019
11◇	231	051	11	198	018
12◇	218	038	12	193	013
13◇	214	034	13	187	007

1	218	038
14●	145	325
15●	126	306
2	22	022
3	194	014
4	203	023
5	210	030
6	208	028
7	210	030
8	206	026
9	216	036
10	212	032
11	213	033
12	215	035
13	215	035
14	205	025
15	207	027
16	223	043
16●	171	351
17	222	042
18	214	034
17●	175	355
19	202	022
20	209	029
21	216	036
22	206	026
23	217	037
24	179	359
25	21	021
26	201	021
27	224	044
28	245	065
29	206	026
30	211	031

14	186	006
15	192	012
16	201	021
17	227	047
18	198	018
19	200	020
20	189	009
21	205	025
22	196	016
23	204	024
24	204	024
25	207	027
26	197	017
27	205	025
28	200	020
29	197	017
30	206	026
31	196	016

Scanline E fracture attitudes			Scanline F fracture attitudes		
Fracture Number	**Strike**	**Strike's northerly reading**	**Fracture Number**	**Strike**	**Strike's northerly reading**
1	188	008	1	196	016
2	201	021	2	020	020
3	200	020	3	186	006
4	188	008	4	195	015
5	201	021	5	016	016
◇1	001	001	6	205	025
6	016	016	7	021	021
◇2	163	343	8	177	357
7	200	020	9	020	020
◇3	162	342	10	222	042
8	200	020	11	024	024
9	201	021	12	199	019
10	194	014	13	020	020
11	206	026	14	029	029
◇4	164	344	15	018	018
12	195	015	16	025	025
13	204	024	17	202	022
14	205	025	18	194	014
			19	019	019
			20	019	019
			21	027	027
			22	014	014
			23	185	005
			24	173	353
			25	176	356
			26	195	015
			27	158	338
			28	156	336
			29	173	353
			30	176	356
			31	174	354
			32	186	006
			33	179	359
			34	179	359
			35	181	001
			36	177	357
			37	185	005
			38	010	010
			39	195	015

Scanline G fracture attitudes			Scanline H fracture attitudes		
Fracture Number	**Strike**	**Strike's northerly reading**	**Fracture Number**	**Strike**	**Strike's northerly reading**
1	145	325	1	211	031
2	059	059	2	203	023
3	246	066	3	202	022
4	246	066	4	207	027
5	218	038	◇1	038	038
6	202	022	5	214	034
7	212	032	6	056	056
8	110	290	◇2	127	307
9	223	043	7	038	038
10	241	061	8	233	053
11	216	036	9	210	030
12	220	040	10	220	040
13	219	039	11	211	031
14	228	048	12	233	053
15	224	044	13	038	038
16	237	057	14	031	031
17	211	031	15	228	048
18	206	026	16	228	048
19	208	028	17	046	046
20	219	039	18	029	029
21	203	023	19	214	034
22	203	023	20	216	036
23	207	027	21	217	037
24	204	024	22	235	055
25	N/A	N/A	23	044	044
			24	042	042
			25	034	034
			26	209	029
			27	028	028
			28	201	021
			29	198	018
			30	218	038
			31	221	041

Appendix C: Schmidt Hammer Data

	J_{NO}-1_L	J_{NB}-2_L	J_{NB}-3_L	J_{NO}-4_U	J_{NB}-5_U	J_{NB}-6_M	J_{NB}-9_M
1	55.5	36.5	45	51.5	36	17.5	36
2	56	39.5	42.5	48.5	38.5	47.5	24.5
3	55	36	43	46	40.5	48	34
4	56	37.5	44.5	48	29.5	42.5	30
5	61	37	46.5	46	29	33.5	34.5
6	61	38	41	49	49.5	48	32
7	54.5	39.5	33.5	48	23.5	44	33
8	54.5	39	39	46	29	35.5	32
9	51.5	31	34.5	44.5	29	43.5	26.5
10	52	37.5	35	45.5	44	46	35.5
Mean	55.7	37.2	40.5	47.3	34.8	40.6	31.8
Standard Deviation	3.2	2.5	4.7	2.1	8.2	9.5	3.8
Max	61	39.5	46.5	51.5	49.5	48	36

Table 15: All Schmidt Hammer rebound value data collected at sample locations in the Navajo Sandstone.

Appendix D: Petrographic Data

Sample	BS18-01 (Figure 19)
Minerals, dominant	Quartz (90%)
Minerals, trace	Plagioclase (4%) Pyroxene (1%) Orthoclase (5%)
Grain size	Fine sand
Sorting	Poor to moderate
Roundness	Subangular to subrounded with a couple rounded or angular
Sphericity	Low with a couple high
Compositional maturity	Mature
Textural maturity	Submature to mature
Grain contacts	Most planar, some point and suture
Cement	Iron oxides, potentially epoxy
Deformation features	microfractures, crushed grains

Table 16: Data collected from thin section sample BS18-01, made from BS18-J_{NO}-1_{L}.

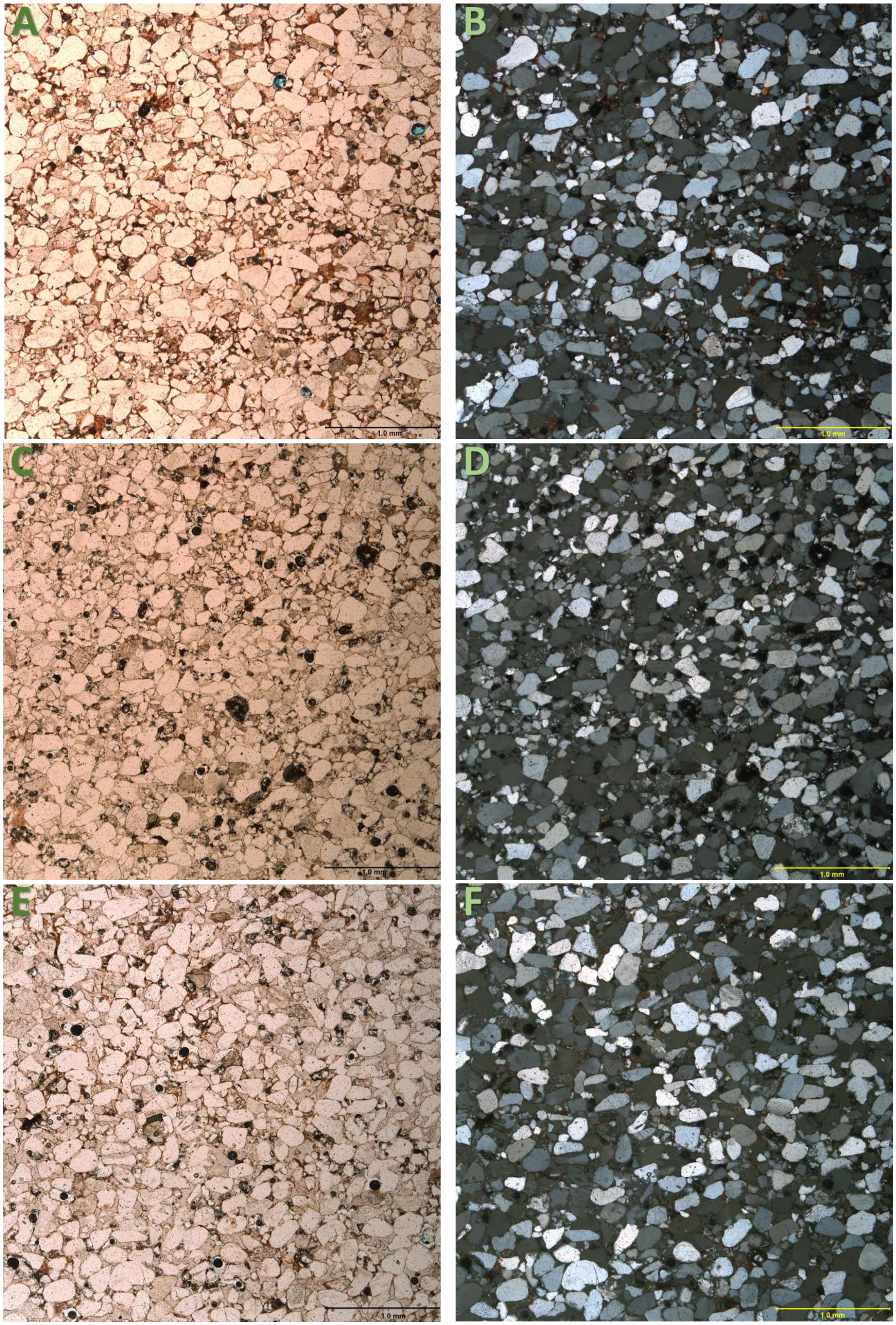

Figure 19: Photomicrograph of thin section BS18-01. Magnification 4x, scale bar 10 mm.

Sample	BS18-02 (Figure 20)
Minerals, dominant Minerals, trace	Quartz (99%) Plagioclase (1%) one grain of pyroxene
Grain size Sorting Roundness Sphericity	Medium sand Well Subrounded with some rounded Moderate to high
Compositional maturity Textural maturity	Supermature Supermature
Grain contacts	Point and Planar
Cement	Epoxy
Deformation features	microfractures, crushed grains

Table 17: Data collected from thin section sample BS18-02, made from BS18-J_{NB}-2_L.

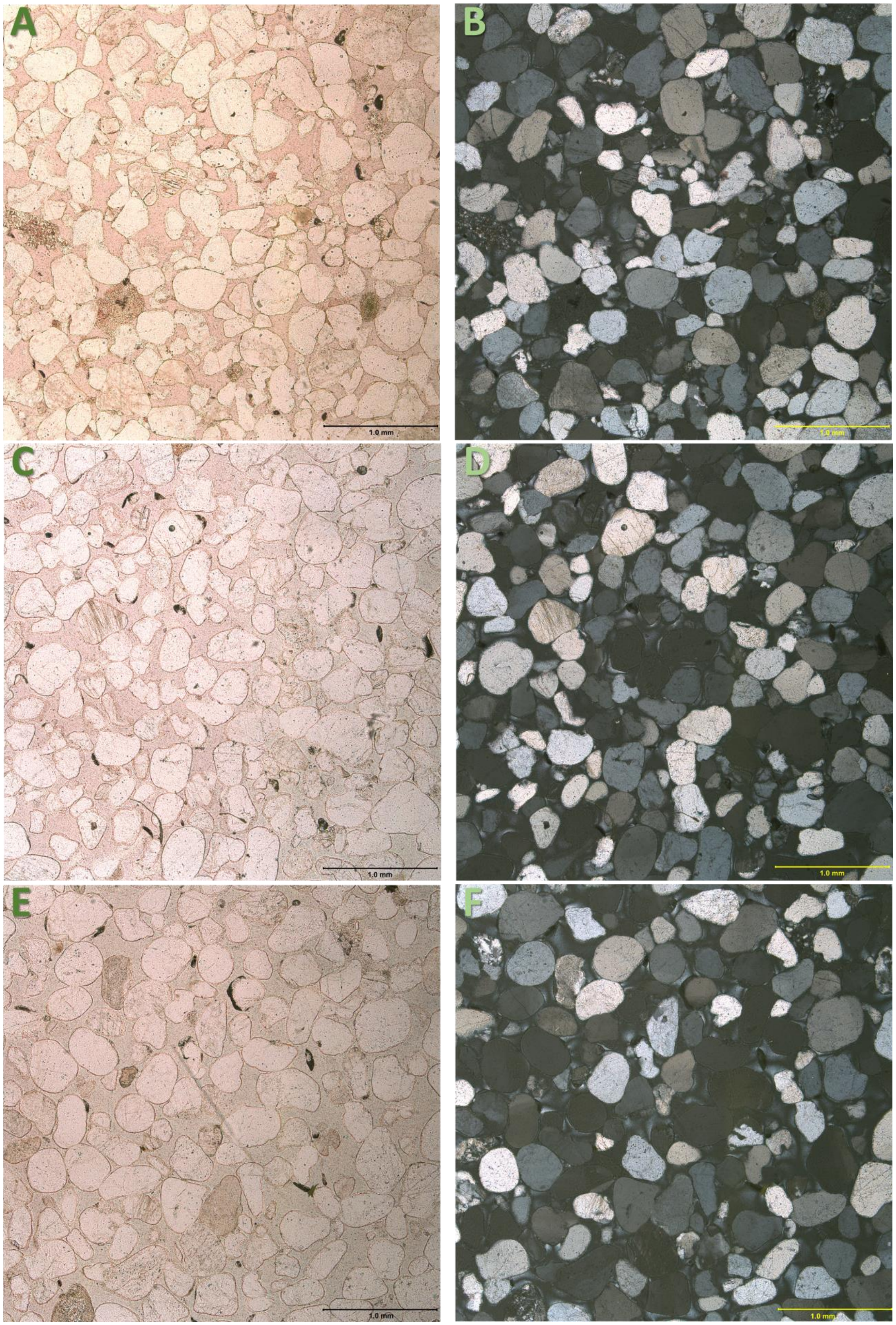

Figure 20: Photomicrograph of thin section BS18-02. Magnification 4x, scale bar 1.0 mm.

Sample	BS18-03 (Figure 21)
Minerals, dominant Minerals, trace	Quartz (96%) Sericite? (1%) Plagioclase (3%)
Grain size Sorting Roundness Sphericity	Fine sand Moderate Subangular to subrounded with some angular Low
Compositional maturity Textural maturity	Supermature Mature
Grain contacts	Planar
Cement	Epoxy?
Deformation features	microfractures, crushed grains, potential pattern in orientation of planar contacts

Table 18: Data collected from thin section sample BS18-03, made from BS18-J_{NB}-3_{L}.

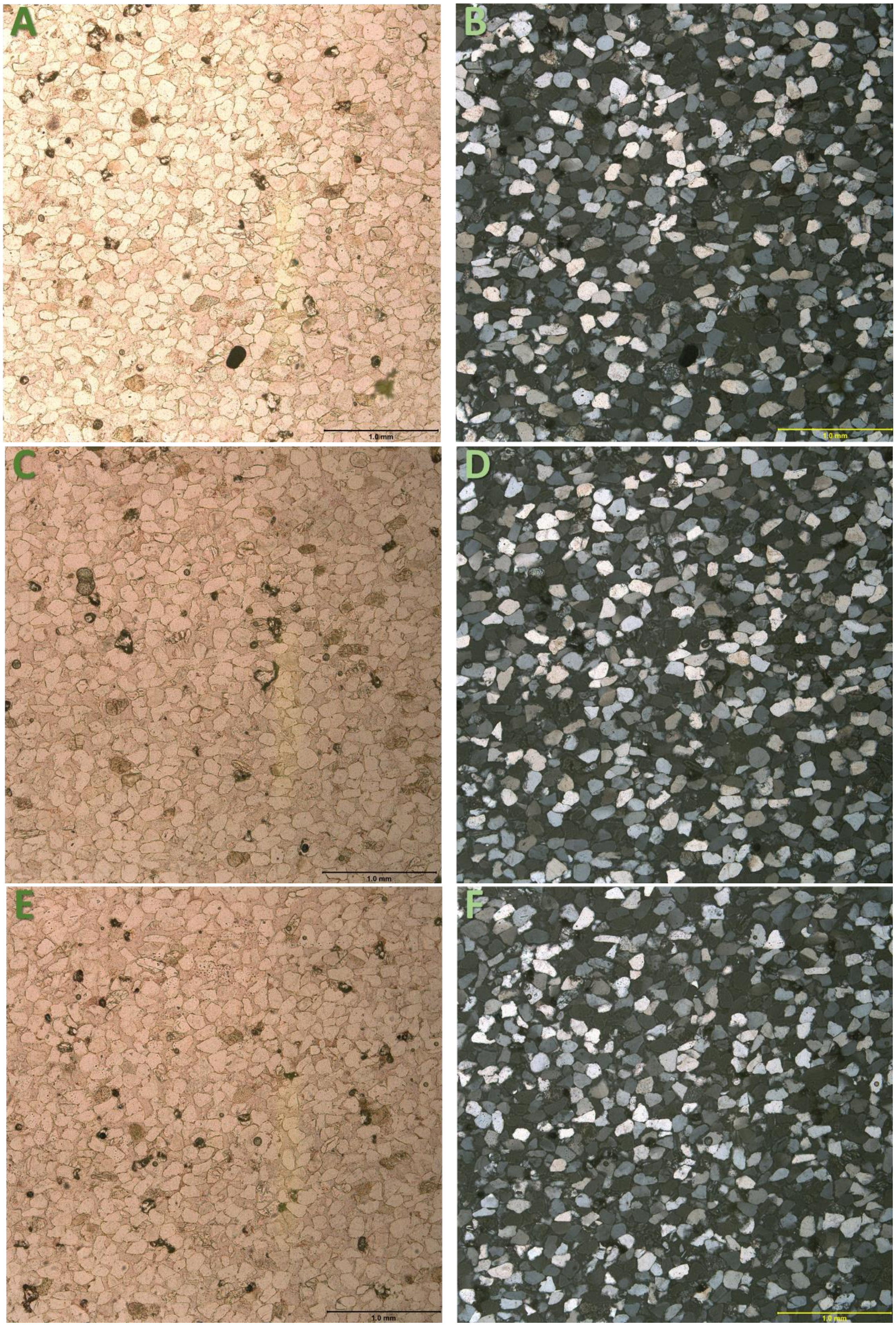

Figure 21: Photomicrograph of thin section BS18-03. Magnification 4x, scale bar 1.0 mm.

Sample	BS18-04 (Figure 22)
Minerals, dominant Minerals, trace	Quartz (96%) Plagioclase (1%) Pyroxene (1%) Orthoclase (2%) mystery mineral
Grain size Sorting Roundness Sphericity	Fine to very fine sand Moderate Subangular to subrounded with some angular Low
Compositional maturity Textural maturity	Supermature Mature
Grain contacts	Most planar and point with some concavo/convex
Cement	Iron oxides
Deformation features	microfractures, crushed grains

Table 19: Data collected from thin section sample BS18-04, made from BS18-J_{NO}-4_{U}.

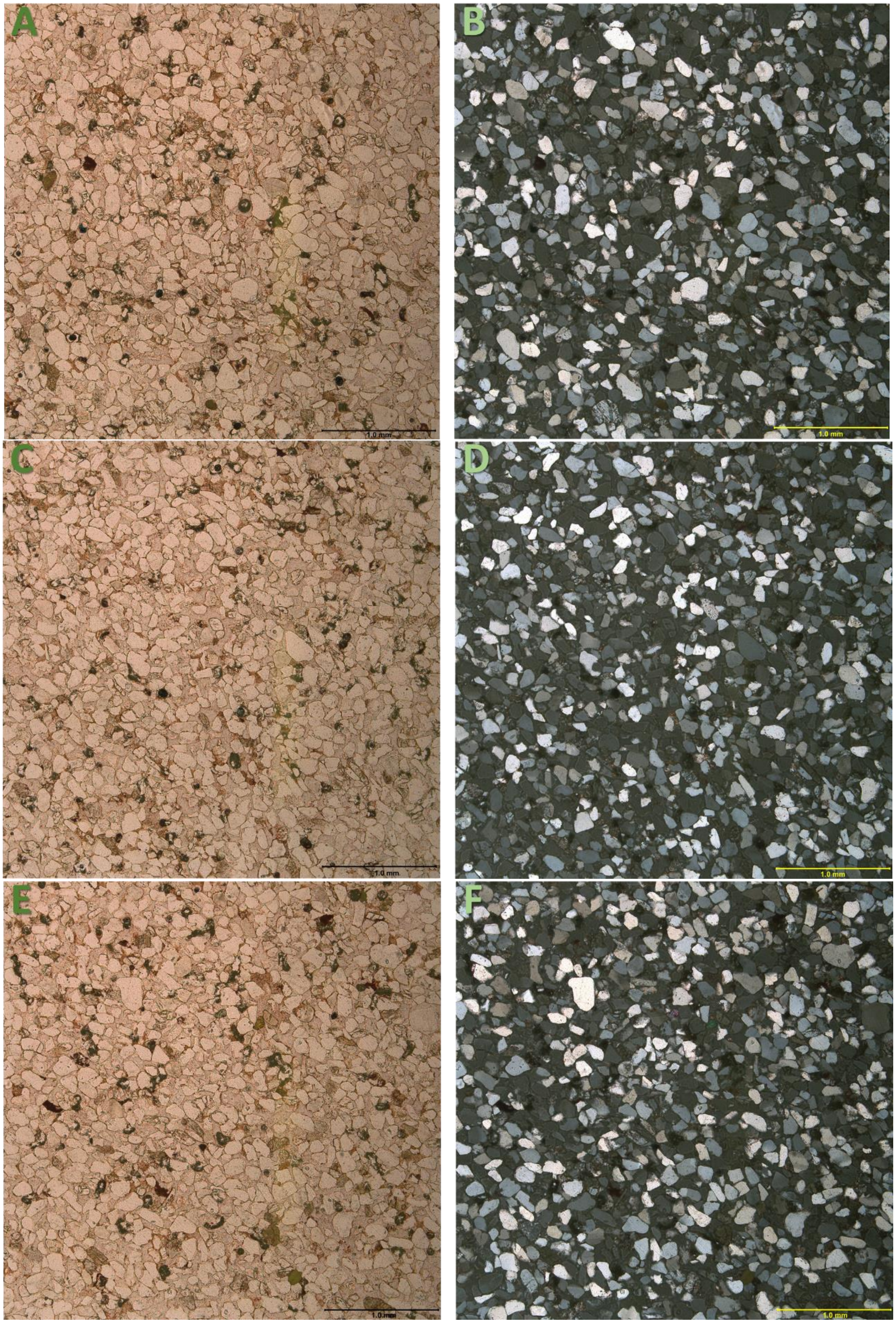

Figure 22: Photomicrograph of thin section BS18-04. Magnification 4x, scale bar 1.0 mm.

Sample	BS18-05 (Figure 23)
Minerals, dominant Minerals, trace	Quartz (96%) Plagioclase (3%) Orthoclase (1%)
Grain size Sorting Roundness Sphericity	Medium sand Poor Subangular to rounded Low with some high
Compositional maturity Textural maturity	Supermature Submature
Grain contacts	Point, planar, and concavo/convex
Cement	Epoxy
Deformation features	microfractures, crushed grains, cracked grains, cracks caused by visible point contacts

Table 20: Data collected from thin section sample BS18-05, made from BS18-J_{NB}-5_{U}.

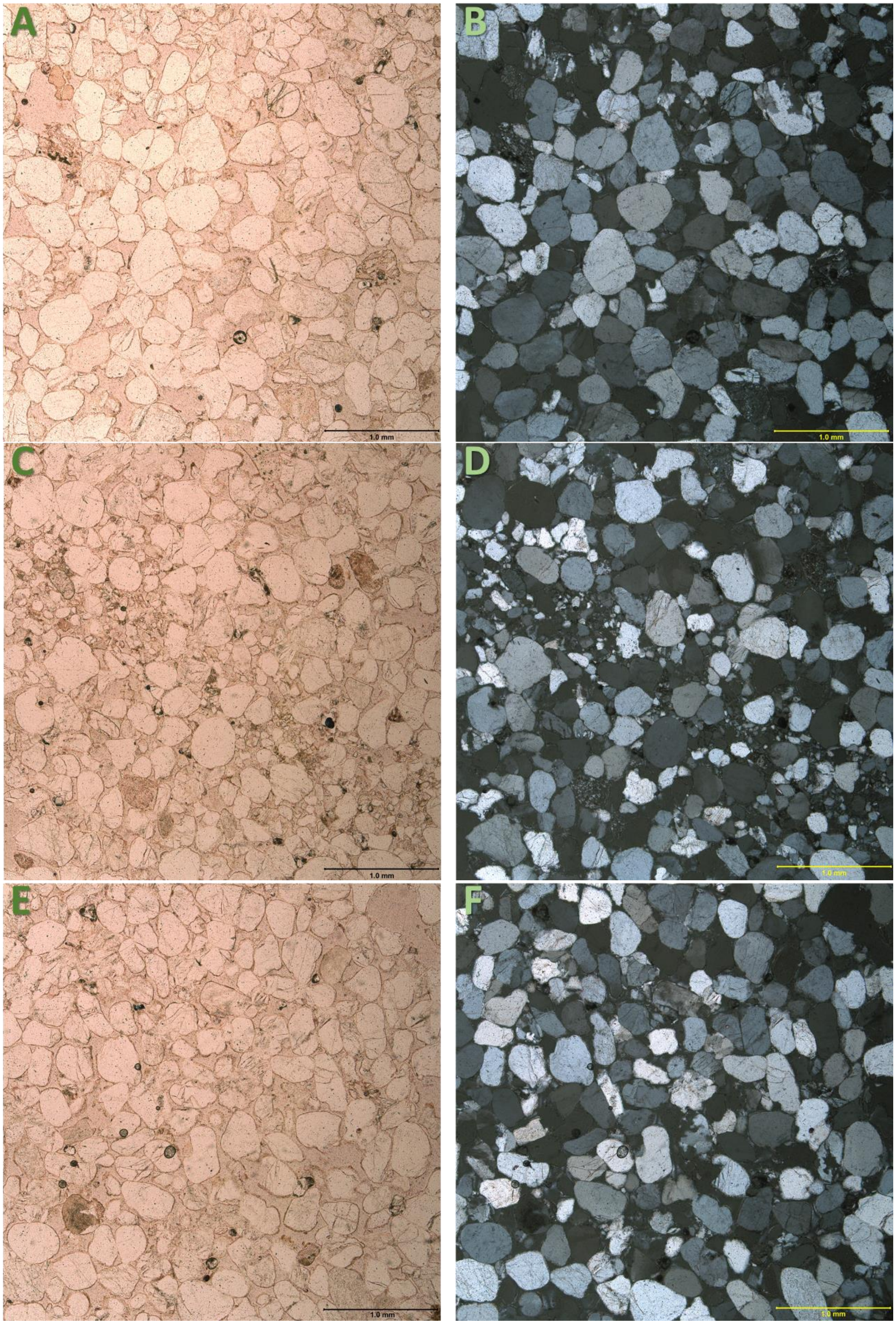

Figure 23: Photomicrograph of thin section BS18-05. Magnification 4x, scale bar 1.0 mm.

Sample	BS18-06 (Figure 24)
Minerals, dominant Minerals, trace	Quartz (96%) Pyroxene (1%) Plagioclase (3%)
Grain size Sorting Roundness Sphericity	Medium to fine sand Moderate Subangular to subrounded Low
Compositional maturity Textural maturity	Supermature Mature
Grain contacts	Most planar, some point and concavo/convex
Cement	Iron oxides Epoxy
Deformation features	microfractures, possible deformation bands that are smaller grained and more compact with more iron content

Table 21: Data collected from thin section sample BS18-06, made from BS18-J$_{NB}$-6$_{M}$.

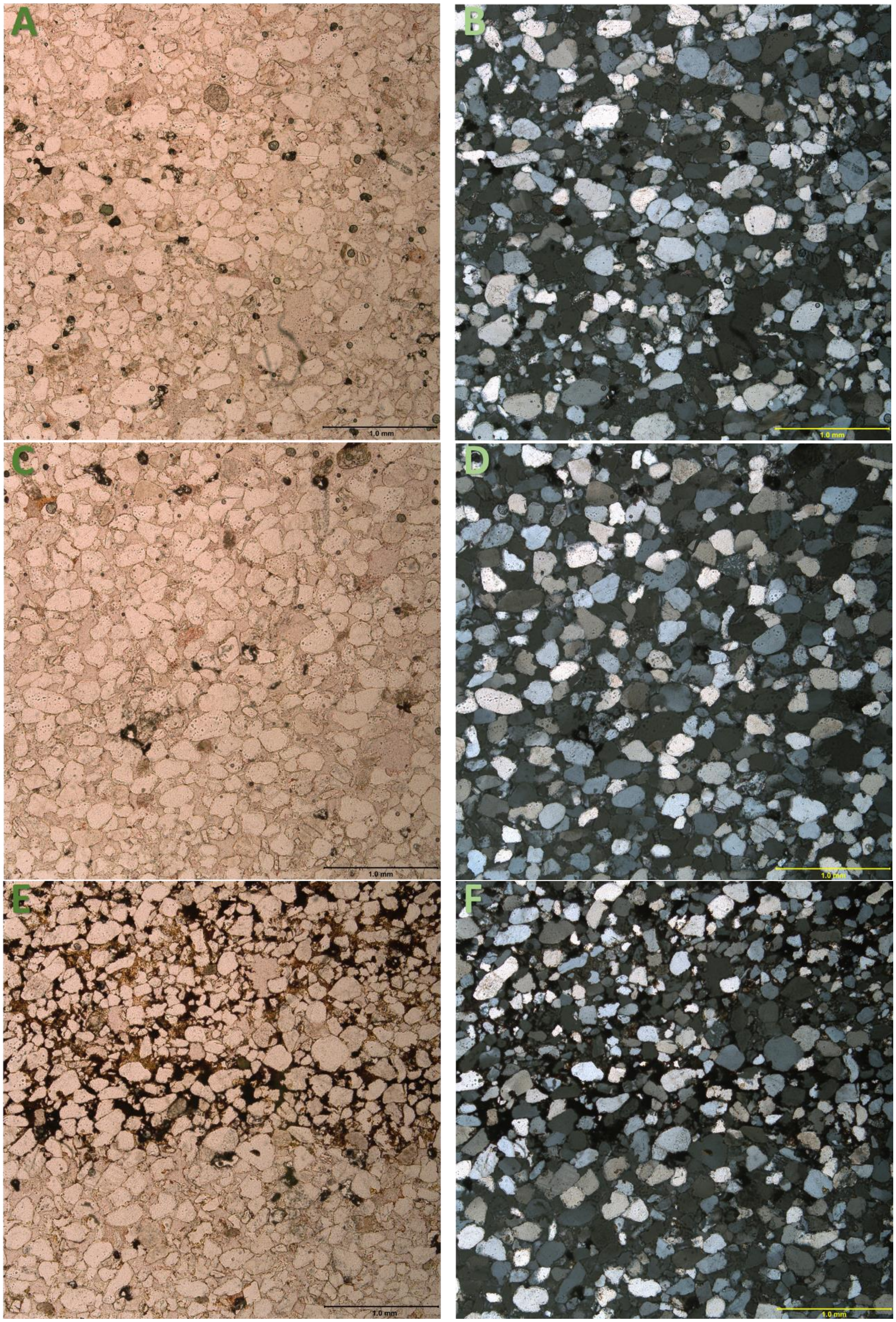

Figure 24: Photomicrograph of thin section BS18-06. Magnification 4x, scale bar 1.0 mm.

Sample	BS18-09 (Figure 25)
Minerals, dominant Minerals, trace	Quartz (97%) Plagioclase (2%) Orthoclase (1%)
Grain size Sorting Roundness Sphericity	Medium to coarse sand Well Subrounded to rounded with some subangular High with some low
Compositional maturity Textural maturity	Supermature Supermature
Grain contacts	Point and planar
Cement	Iron oxides Epoxy
Deformation features	microfractures, broken grains

Table 22: Data collected from thin section sample BS18-09, made from BS18-J_{NB}-9_{M}.

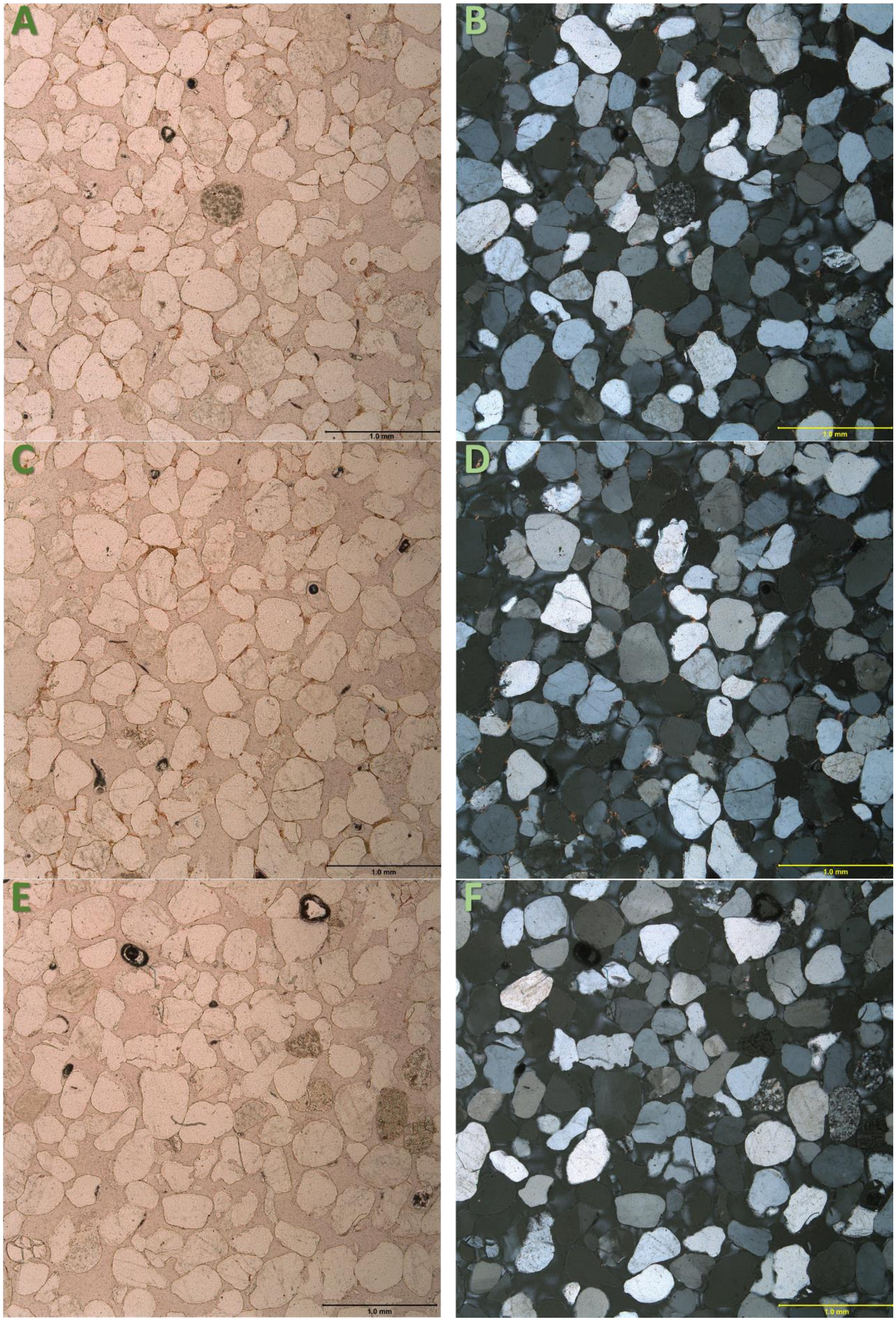

Figure 25: Photomicrograph of thin section BS18-09. Magnification 4x, scale bar 1.0 mm.

Sample	BS18-10 (Figure 26)
Minerals, dominant	Quartz (97%)
Minerals, trace	Plagioclase (1%) Pyroxene (1%) Biotite (1%)
Grain size	Medium to fine sand with some coarse and very fine
Sorting	Poor
Roundness	Subangular to subrounded with some rounded
Sphericity	Low
Compositional maturity	Mature
Textural maturity	Submature to mature
Grain contacts	Point and planar, less planar than other samples
Cement	Iron oxides?
Deformation features	microfractures, layers/lines, severely cracked grains

Table 23: Data collected from thin section sample BS18-10, made from BS18-J_N-10.

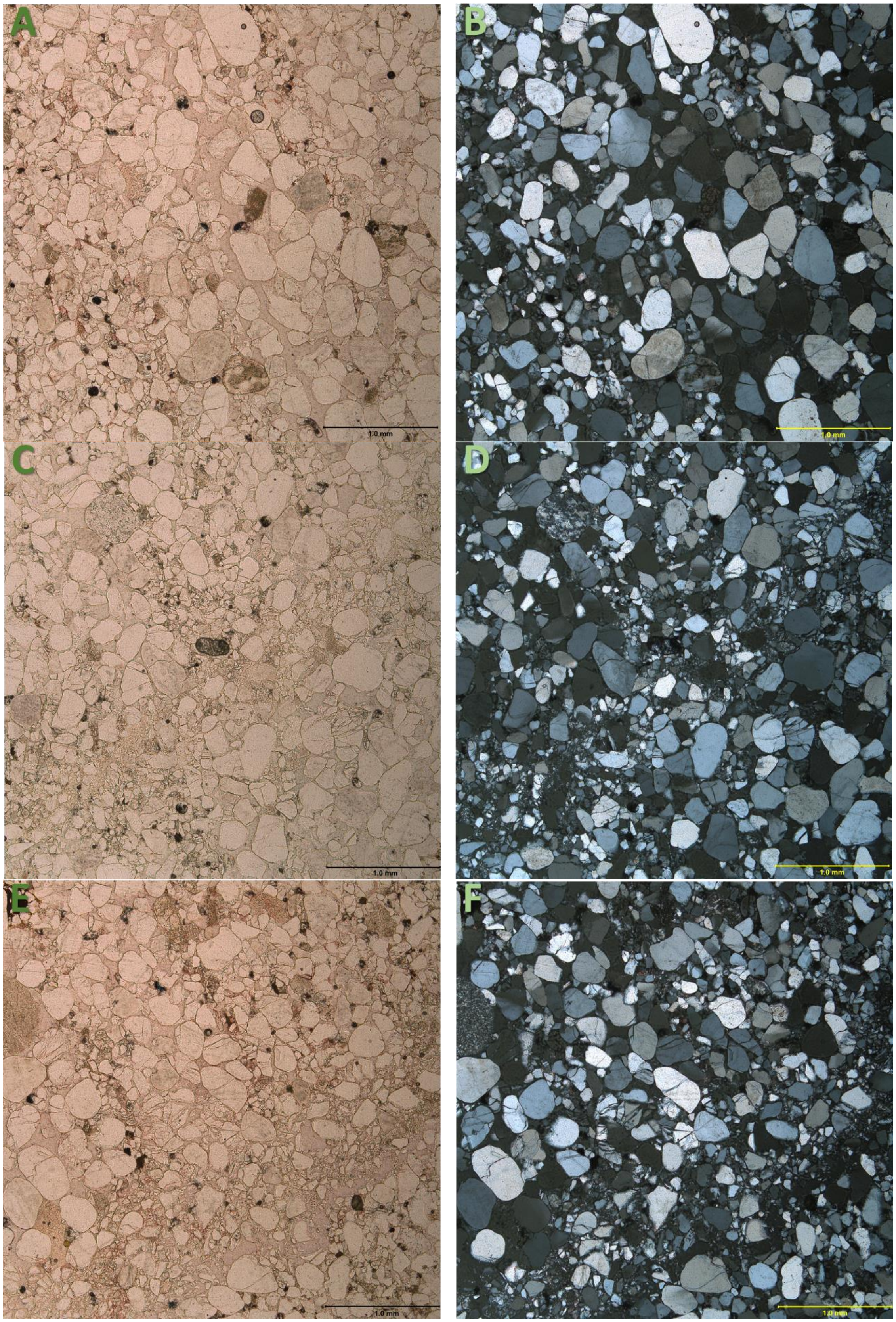

Figure 26: Photomicrograph of thin section BS18-10. Magnification 4x, scale bar 1.0 mm.

Sample	BS18-11 (Figure 27)
Minerals, dominant Minerals, trace	Quartz (99%) Pyroxene (1%)
Grain size Sorting Roundness Sphericity	Mostly fine sand with some coarse Poor Subangular with some angular and rounded Low with some high
Compositional maturity Textural maturity	Supermature Submature
Grain contacts	Point
Cement	Epoxy?
Deformation features	microfractures, broken grains

Table 24: Data collected from thin section sample BS18-11, made from BS18-J_N-11.

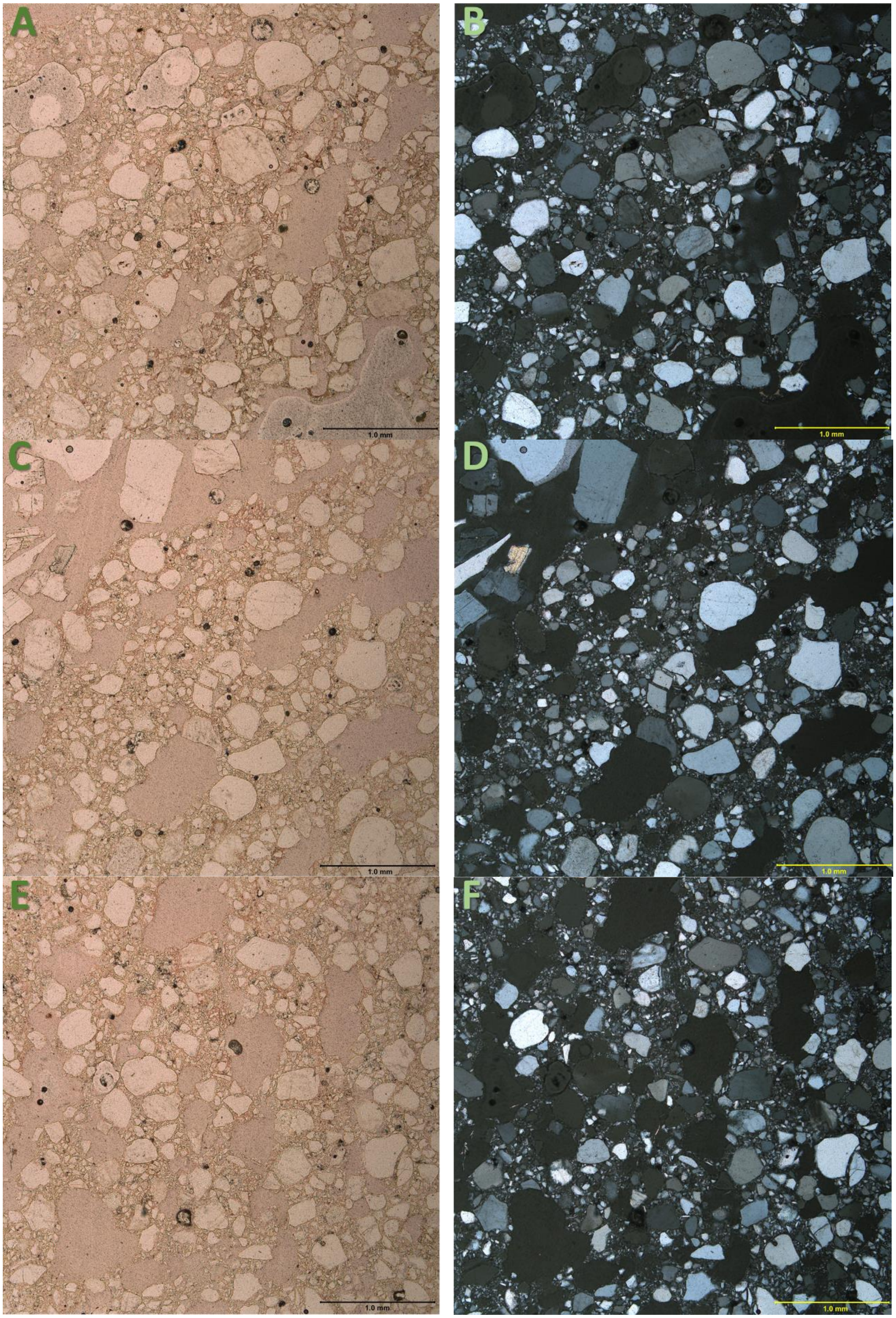

Figure 27: Photomicrograph of thin section BS18-11. Magnification 4x, scale bar 1.0 mm.

Sample	BS18-C1 (Figure 28)
Minerals, dominant Minerals, trace	Quartz (98%) Plagioclase (1%) Pyroxene (1%)
Grain size Sorting Roundness Sphericity	Medium to fine sand with some coarse and very fine Poor Subangular to subrounded with some angular and rounded Low
Compositional maturity Textural maturity	Supermature Submature
Grain contacts	Point and planar
Cement	Iron oxides
Deformation features	microfractures, broken grains, layers/lines

Table 25: Data collected from thin section sample BS18-C1, made from BS18-J_N-C_1.

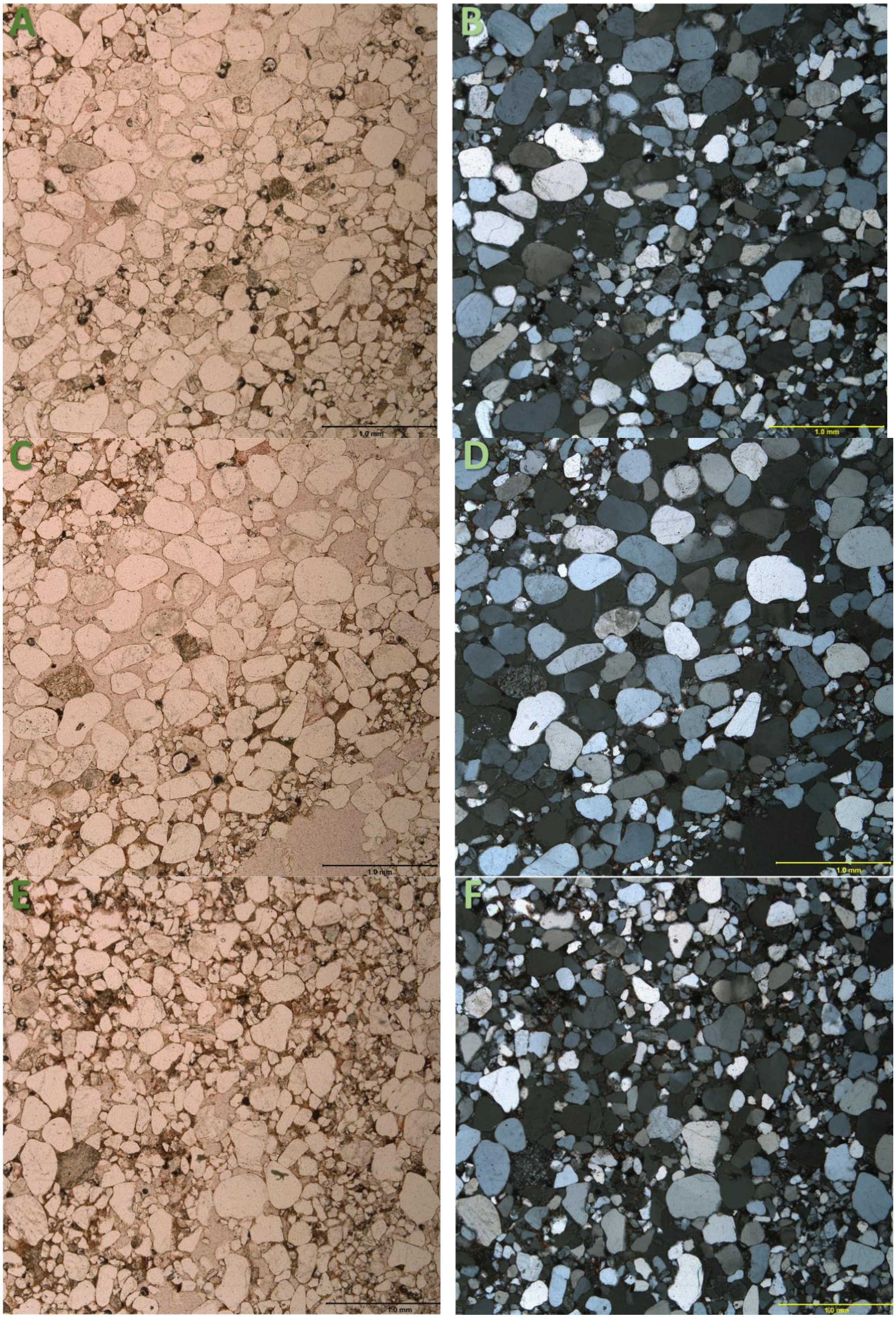

Figure 28: Photomicrograph of thin section BS18-C1. Magnification 4x, scale bar 1.0 mm.

Sample	BS18-C2 (Figure 29)
Minerals, dominant Minerals, trace	Quartz (97%) Orthoclase (1%) Sericite? (1%) Plagioclase (1%)
Grain size Sorting Roundness Sphericity	Medium to fine sand Moderate to well Subrounded with some rounded Moderate
Compositional maturity Textural maturity	Mature Mature
Grain contacts	Point and planar
Cement	Iron oxides
Deformation features	microfractures, cracked grains

Table 26: Data collected from thin section sample BS18-C2, made from BS18-J_N-C_2.

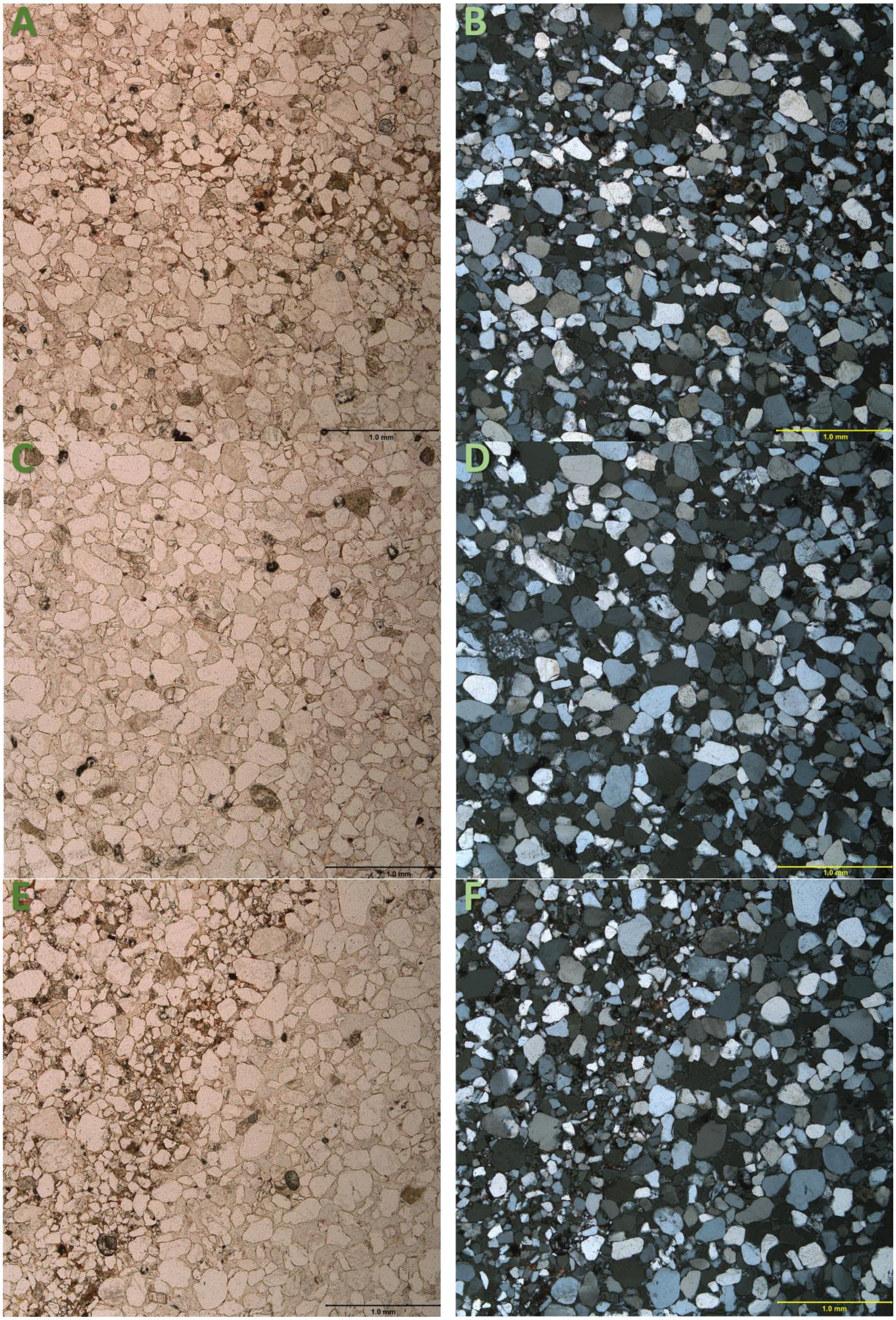

Figure 29: Photomicrograph of thin section BS18-C2. Magnification 4x, scale bar 1.0 mm.

Sample	BS18-C3 (Figure 30)
Minerals, dominant Minerals, trace	Quartz (96%) Plagioclase (2%) Orthoclase (1%) Pyroxene (1%)
Grain size Sorting Roundness Sphericity	Medium sand Moderate Subrounded with some subangular and rounded Moderate
Compositional maturity Textural maturity	Mature Mature
Grain contacts	Point and planar
Cement	Iron oxides
Deformation features	microfractures, cracked grains

Table 27: Data collected from thin section sample BS18-C3, made from BS18-J_N-C_3.

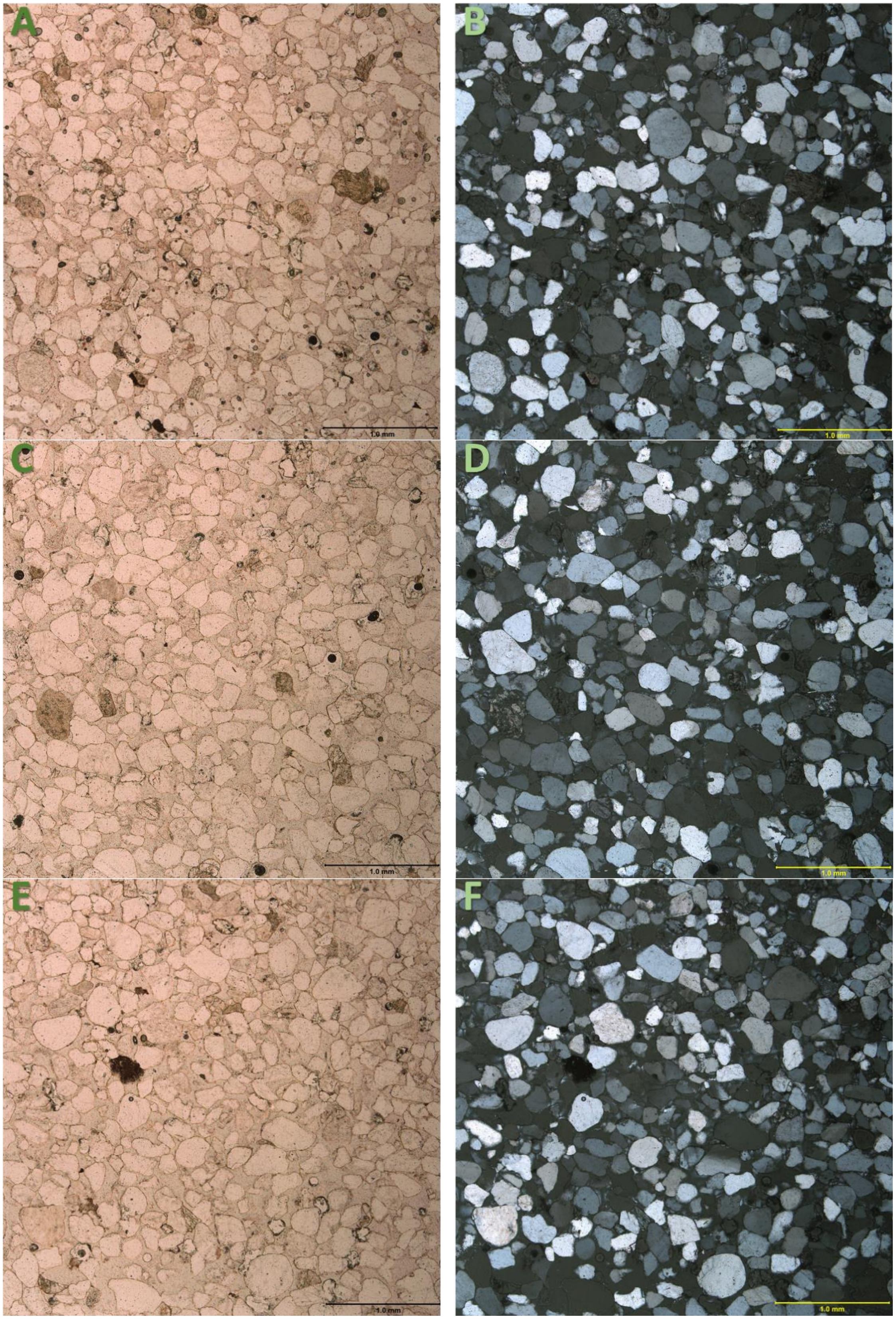

Figure 30: Photomicrograph of thin section BS18-C3. Magnification 4x, scale bar 1.0 mm.